MBE Growth and Characterization of $Zn_{1-x}Cr_xTe$ Diluted Magnetic Semiconductor

HOU XIUJUAN

(B. Eng.(Hons.), NTU)

A THESIS SUBMITTED

FOR DEGREE OF MASTER OF ENGINEERING

DEPARTMENT OF ELECTRICAL & COMPUTER ENGINEERING

NATIONAL UNIVERSITY OF SINGAPORE

2005

ACKNOWLEDGEMENT

I would like to take this opportunity to express my sincere gratitude and appreciation to my supervisors Dr. Thomas Liew from DSI and Dr. Teo Kie Leong from ISML. I would like to thank Dr. Liew for his valuable advices for the project analysis and the efforts of arranging the characterization equipment trainings. I would like to thank Dr. Teo for his kind and consistent concern, support and guidance in the project and also all the valuable discussion on the experimental results. I also benefit a lot from the discussion with Dr. Bae Seongtae.

I am also grateful to be in a caring, supportive and cooperative research team. I thank Mr. M. G. Sreenivasan, Mr. Ko Viloane and Ms. Chen Wenqian for their support and help in this project. I would like to thank Seng Ghee, Randall, Sunny, Yingzi, Saurabh, Jon and the whole Spintronic group of DSI for the valuable discussion and all the fun.

I would like to express my appreciation for all the staffs in DSI and ISML for their help in carrying out the experiments, especially to Ms. Loh Fong Leong, Mr. Alaric Wong, Ms Tan Bee Ling, Mr. Zhao Haibao, Dr. Qiu Jinjun, Dr Guo Zaibing and Mr. Chong Joon Fatt. I would like to thank the students, Ms Maureen Tay, Ms Doris Ng and Mr. Li Hongliang, who have helped me even in their busy study.

I would like to thank all of friends and my parents for their support during my master study period. Last but not least, I thank God for His peace and joy in my life.

TABLE OF CONTENTS

SUMMARY

Diluted magnetic semiconductor (DMS) is the key for practical spintronics, which utilizes the spin property of electrons. DMS is a family of materials that encompasses standard semiconductors, in which a sizable portion of atoms are substituted by elements that produce magnetic moments (magnetic atoms) in a semiconductor matrix. The realization of this kind of material at or higher than room temperature will enable new functions in new devices.

There are three DMS systems that exhibit ferromagnetic order unambiguously, namely GaMnAs, InMnAs and ZnCrTe. The previous two III-V based DMS have been intensely studied but the achieved Curie temperature (T_c) is well below room temperature. Cr doped ZnTe is the first confirmed DMS with above-room temperature Curie temperature. The motivation of this project is to grow high T_c Cr doped ZnTe thin film using the solid-source molecular beam epitaxy (MBE) and study the properties of the grown films.

We have used different characterization methods to study the various properties of this DMS system. The structure properties of the samples were studied through *in-situ* RHEED pattern observation and the measurements of X-Ray Diffraction (XRD), Atomic Force Microscope (AFM) and Scanning Electron Microscopy (SEM). Vibrating Sample Magnetometer (VSM) and Superconducting Quantum Interference Device (SQUID) were used to access the magnetic properties of the samples. The composition of the samples was measured by Energy Dispersive X-ray Spectrometer (EDX) and Particle Induced X-Ray Emission (PIXE).

In this project, the growth condition for epitaxial film was optimized through changing the substrate temperature and flux ratio of Zn/Te and Cr/Te. Before the growth of ZnCrTe, a 40nm thick ZnTe buffer layer was deposited with the Zn/Te flux ratio varying from 1.2 to 2.7 at different substrate temperature (200^{o}C to 250^{o}C). The Cr/Te flux ratio was varied from 0.004 to 0.3. Curie temperatures varying from 55K to 265K can be achieved through doping with different concentration of Cr.

In this project the highest T_c achieved for $Zn_{1-x}Cr_xTe$ thin film is 265K with Cr concentration of 14% from PIXE measurement. From the linear relationship between T_c and Cr concentration, films with above room Curie temperature could be achieved with Cr doping concentration of 20%. This showed that our results are consistent with results of Saito *et al.*.

$Cr_{1-\delta}Te$ precipitate with strong magnetization and Curie temperature of 365K was also observed in this project. From our thorough literature study of $Cr_{1-\delta}Te$, the strong magnetization observed could be from monoclinic Cr_3Te_4 precipitates. The study of this precipitate helps to understand the Cr doped ZnTe system.

LIST OF TABLES

LIST OF FIGURES

Chapter 1: Introduction

1.1 Background

Electronics comprise a great part of our world and semiconductor is the base of our daily electronic products. Various electronic devices are operated by manipulating electrical charges, especially integrated circuits and high-frequency devices made of semiconductors. They are widely used for information processing and communications by making use of the charge of electrons in semiconductors [1]. The spin of the electron as another property of the electron is utilized in the mass storage of information field; however, only the spin of electrons in ferromagnetic materials, such as Fe, Co, Ni and other compound magnets, is made used of. It is then quite natural to ask if both the charge and spin of electrons can be used to further enhance the performance of devices [1]. For this reason, a new technical term, spintronics, emerged since the discovery of Giant Magnetoresistance (GMR) in 1988. Generally, spintronics refers to spin transport electronics or spin based electronics. In this case, the electron spin will substitute electron charges to carry information, and this offers opportunities for a new generation of devices combining standard microelectronics with spin-dependent effects. By manipulating the electron spin and the charge we may be able to inject spin-polarized current into semiconductors to control the spin state of carriers, that may allow us to carry out qubit (quantum bit) operations required for quantum computing [2].

One of the major technical barriers that must be overcome to realize the practical implementation of semiconductor-based spintronic devices is the development of suitable

spin-polarized materials that will effectively allow spin-polarized carriers to be injected, transported, and manipulated in semiconductor heterostructures at room temperature. Also, the availability of such materials will facilitate a wider range of device configurations [3].

In fact, the researchers have started the research on semiconductors which are also ferromagnetic back in the 1960s and early 1970s, although the interest on this research is not continuous. Eu-based chalcogenide materials which exhibited ferromagnetism were found with Curie temperature around 50 K or less [3]. However Eu-based chalcogenide has rather poor semiconducting transport properties so it is not suitable for spintronic usage. Along the way, magnetically doped II–VI ternary and quarternary semiconductor alloys, e.g. CdMnSe, CdMnTe, PbSnMnTe and others were studied. However, most of these materials exhibited spin glass or related disordered magnetic behavior and any ferromagnetism invariably had very low (~5 K) transition temperature [4]. Then the idea of a diluted magnetic semiconductor (DMS) was proposed. In the DMS system, the cation sites of the host semiconductor are substituted by a small concentration of magnetically active atoms. Generally, the belief is the *s,p-d* exchange should be the source of magnetism inside DMS. More excitingly, according to Dietl group's Zener Model [5], Curie temperature above room temperature can be achieved for p-type GaN and ZnO doped with 5% Mn and with 3.5×10^{20} holes/cm^3 [See Fig 1]. Surely this result encouraged a lot of people to continue on the search of new ferromagnetic semiconductor materials with above room Curie temperature.

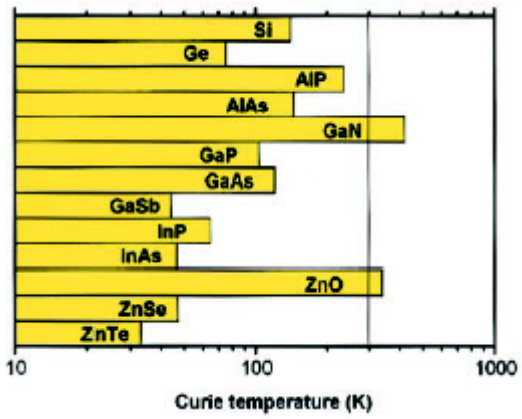

Fig 1-1. Computed values of the Curie temperature T_c for various p-type semiconductors containing 5% of Mn and 3.5× 10^{20} holes per cm^3 [5].

However, over the years of research, practical Mn doped DMS has not been realized. Although exciting T_c was reported, magnetic precipitates effect cannot be eliminated in those systems. In the meanwhile, the researchers also extend the finding of applicable DMS to other possible materials. II-VI material-based semiconductor, III-V material-based semiconductor, IV-VI materials and oxide-based semiconductors are investigated doping with different transition metals. Making DMS is not easy because the magnetic transition metal (i.e. Mn) is not thermodynamically stable in the semiconductor host (e.g. GaAs), and tends to segregate [4]. Moreover, the crystal structures of magnetic materials are usually quite different from that of the semiconductors used in electronics. As these crystal structures are mostly not the stable state with lowest state energy, it makes the growth of DMS more difficult since crystal with lowest energy state is easy to form in the structure. Although there are a lot of difficulties in preparing well-structured DMS, it can be synthesized under non-equilibrium conditions.

In order to use DMS in spintronic device, more research is required in order to understand the magnetic mechanism behind DMS and in fabrication of high T_c DMS. In

general, the field of semiconductor spintronics is still in its infant stage and holds vast opportunities for research.

1.2 Current Issues and Motivation

Among the various DMS materials, III–V $Ga_{1-x}Mn_xAs$ and $In_{1-x}Mn_xAs$ DMS thin films grown on GaAs substrates have been the most extensively studied. However, the highest Curie temperature of GaMnAs system and InMnAs are ~110K [6] and ~35K [7] only, which are well below room temperature. The search for DMS with high Curie temperature is thus a very attractive area in spintronics research. Great efforts have been devoted to the synthesis and characterization of different types of DMS materials. Although room temperature ferromagnetism has been reported in many systems, such as GaN:Mn [8–17] GaN:Cr [18,19] TiO_2:Co [20] ZnO:Co [21] $CdGeP_2$:Mn [22] and ZnO:Mn [23,24] and the reported T_c can be as high as 940K [10]; however those results are not well-verified. The existence of ferromagnetic precipitates cannot be possibly ignored.

Recently, magnetic circular dichroism (MCD) measurement has been used to clarify the origin of ferromagnetism in DMS systems. Magneto-optical spectroscopy is the direct method for evaluating the *s,p – d* exchange interactions of DMS [25]. The *s,p – d* exchange interactions induce a spin-dependent modification of the host semiconductor band structure, that is, the Zeeman splitting. The MCD intensity is proportional to the Zeeman splitting. Therefore magneto-optical spectroscopy can be used to confirm the intrinsic ferromagnetism of DMS [25]. To the best of our knowledge, three DMS systems

that exhibit ferromagnetic ordering unambiguously are GaMnAs [26] InMnAs [27] and ZnCrTe [28-32]. As mentioned before, the former two are the prototype DMS in III-V family and have been studied extensively. The last one is the first II-VI DMS where high-T_c ferromagnetism is reliably detected. Saito *et al.* [30-32] has succeeded in synthesizing a $Zn_{1-x}Cr_xTe$ thin film with 20% Cr doped using molecular-beam epitaxy. Room temperature ferromagnetism was observed in the sample they prepared.

More theoretical studies on this novel $Zn_{1-x}Cr_xTe$ DMS are inspired by the experimental results. The theoretical study shows that the origin of the ferromagnetism in (Zn, Cr)Te is ferromagnetic *s,p-d* exchange interaction [33-35]. Ozaki *et al.* has declared a linear relationship between T_c and Cr-doping concentration for their samples prepared using MBE system [36-37], the extrapolation of which gives T_c of 300 K for $x = 0.2$. However, Pekarek et al. has presented bulk Cr-doped ZnTe samples, which were prepared by vertical Bridgmen method, exhibiting T_c of 365 K with Cr-doping concentration of 0.0033 [38]. They suggested the ferromagnetic property may be due to some precipitates, such as $Zn_xCr_yTe_z$ or $Cr_{1-\delta}Te$ inside the Cr doped ZnTe system. All these findings suggest more efforts are needed in order to understand the $Zn_{1-x}Cr_xTe$ system and to improve the T_c of this DMS system.

1.2 Objectives

The first objective of this project is to optimize the MBE growth parameters to obtain Zinc-blend structure DMS, namely, Cr doped ZnTe with higher Curie temperature. The second objective of this project is to study the Cr doped ZnTe system including the possible precipitates inside the system. In order to help us understand the magnetic mechanism inside the system, magnetic properties and structural properties are investigated through various measurements. The equipment used include Vibrating Sample Magnetometer (VSM), Superconducting Quantum Interference Device (SQUID), High Resolution X-Ray Diffraction (HRXRD), Atomic Force Measurement (AFM), Scanning Electron Microscopy (SEM), Energy Dispersive X-ray Spectrometer (EDX) and Particle Induced X-Ray Emission (PIXE).

1.3 Organization of Thesis

This thesis is organized in the following way:

Chapter one gives a brief introduction of this project. The background and current issues of DMS are discussed. Chapter two provides some theoretical background; mainly on the literature survey on the current topics of DMS. Chapter three briefly presents the MBE growth process and techniques. Chapter four describes the various characterization tools used in this project. In chapter five, the results and discussion are presented. Chapter six concludes the project and provides some future work aspects.

Reference:

[1] H. Ohno, Science **281**, 951 (1998).

[2] D. P. DiVincenzo, Science **270**, 255 (1995).

[3] Scott A. Chambers and Young K. Yoo, MRS Bulletin (October) 706 (2003).

[4] S. Das Sarma, E. H. Hwang, A. Kaminski, Solid State Commun. **127**, 99 (2003).

[5] T. Dietl, H. Ohno, F. Matsukura, J. Cibert, D. Ferrand, Science **287**, 1019 (2000).

[6] H. Ohno, A. Shen, F. Matsukura, A. Oiwa, A. Endo, S. Katsumoto, and Y. Iye, Appl. Phys. Lett. **69**, 363 (1996).

[7] H. Ohno, H. Munekata, S. von Molnár, and L. L. Chang, J. Appl. Phys. **69**, 6103 (1991).

[8] M. L. Reed, M. K. Ritums, H. H. Stadelmaier, M. J. Reed, C. A. Parker, S. M. Bedai, and N. A. El-Masry, Mater. Lett. **51**, 500 (2001).

[9] M. L. Reed, N. A. El-Masry, H. H. Stadelmaier, M. K. Ritums, M. J. Reed, C. A. Parker, J. C. Roberts, and S. M. Bedair, Appl. Phys. Lett. **79**, 3473 (2001).

[10] S. Sonoda, S. Shimizu, T. Sasaki, Y. Yamamoto, and H. Hori, J. Cryst. Growth **237–239**, 1358 (2002).

[11] T. Sasaki, S. Sonoda, Y. Yamamoto, K. Suga, S. Shimizu, K. Kindo, and H. Hori, J. Appl. Phys. **91**, 7911 (2002).

[12] G. T. Thaler, M. E. Overberg, B. Gila,R. Frazier, C. R. Abernathy, S. J. Pearton, J. S. Lee, S. Y. Lee, Y. D. Park, Z. G. Khim, J. Kim, and F. Ren, Appl. Phys. Lett. **80**, 3964 (2002).

[13] J. M. Lee, K. I. Lee, J. Y. Chang, M. H. Ham, K. S. Huh, J. M. Myoung, W. J. Hwang, M. W. Shin, S. H. Han, H. J. Kim, and W. Y. Lee, Micro- electron. Eng. **69**, 283 (2003).

[14] P. P. Chen, H. Makino, J. J. Kim, and T. Yao, J. Cryst. Growth **251**, 331 (2003).

[15] S. S. A. Seo, M. W. Kim, Y. S. Lee, T. W. Noh, Y. D. Park, G. T. Thaler, M. E. Overberg, C. R. Abernathy, and S. J. Pearton, Appl. Phys. Lett. **82**, 4749 (2003).

[16] Y. Shon, Y. H. Kwon, Sh. U. Yuldashev, Y. S. Park, D. J. Fu, D Y. Kim, H. S. Kim, and T. W. Kang, J. Appl. Phys. **93**, 1546 (2003).

[17] T. Kondo, S. Kuwabara, H. Owa, and H. Munekata, J. Cryst. Growth **237–239**, 1353 (2002).

[18] M. Hashimoto, Y. K. Zhou, M. Kanamura, and H. Asahi, Solid State Commun. **122**, 37 (2002).

[19] S. E. Park, H. J. Lee, Y. C. Cho, S. Y. Jeong, C. R. Cho, and S. Cho, Appl. Phys. Lett. **80**, 4187 (2002).

[20] Y. Matsumoto, M. Murakami, T. Shono, T. Hasegawa, T. Fukumura, M. Kawasaki, P. Ahmet, T. Chikyow, S. Koshihara, and H. Koinuma, Science **291**, 854 (2001).

[21] K. Ueda, H. Tabata, and T. Kawai, Appl. Phys. Lett. **79**, 988 (2001).

[22] G. A. Medvedkin, T. Ishibashi, T. Nishi, K. Hayata, Y. Hasegawa, and K. Sato, Jpn. J. Appl. Phys. **39**, L949 (2000).

[23] S. W. Jung, S. J. An, G. C. Yi, C. U. Jung, S. I. Lee, and S. Cho, Appl. Phys. Lett. **80**, 4561 (2002).

[24] P. Sharma, A. Gupta, K. V. Rao, F. J. Owens, R. Sharma, R. Ahuja, J. M. O. Guillen, B. Johansson, and G. A. Gehring, Nat. Mater. **2**, 673 (2003).

[25] K. Ando, Appl. Phys. Lett. **82**, 100 (2003).

[26] K. Ando, T. Hayashi, M. Tanaka, and A. Twardowski, J. Appl. Phys. **83**, 6548 (1998).

[27] K. Ando, H. Munekata, J. Magn. Magn. Mater **272-276**, 2004 (2004).

[28] H. Saito, V. Zayets, S. Yamagata, and K. Ando, Phys. Rev. B **66**, 081201(2002).

[29] H. Saito, V. Zayets, S. Yamagata, Y. Suzuki, K. Ando, J. Appl. Phys. **91**, 8085 (2002).

[30] H. Saito, V. Zayets, S. Yamagata, and K. Ando, Phys. Rev. Lett. **90**, 207202 (2003).

[31] H. Saito, V. Zayets, S. Yamagata, and K. Ando, J. Appl. Phys. **93**, 6796 (2003).

[32] H. Saito, S. Yamagata, and K. Ando, J. Appl. Phys **95**, 7175 (2004).

[33] Q. Wang, Q. Sun and P. Jena, J. Appl. Phys. **97**, 043904 (2005).

[34] Wen-Hui Xie and Bang-Gui Liu, J. Appl. Phys. **96**, 3559 (2004).

[35] Tetsuya Fukushima, Kazunori Sato, Hiroshi Katayama-Yoshida and P. H. Dederichs, Jpn. J. Appl. Phys. **43**, L1416 (2004).

[36] N. Ozaki, N Nishizawa, S Kuroda and K Takita, J. Phys.: Condens. Matter **16**. s5773 (2004).

[37] N. Ozaki, N. Nishizawa, S. Marcet, S Kuroda and K Takita, J. Superconductivity: Incorporating Novel Magnetism **18**, 29 (2005).

[38] T. M. Pekarek, D. J. Arenas, B. C. Crooker, I. Miotkowski and A. K. Ramdas, J. Appl. Phys. **95**, 7178 (2004).

Chapter 2: Theoretical Background

Each electron in an atom has magnetic moments that originate from both its orbital motion around the nucleus (orbital magnetic moment) and its spin around its axis (spin magnetic moment). Magnetic properties originate from the spin properties of electrons. Coexistence of ferromagnetism and semiconducting properties in Eu chalcogenides and semiconducting spinels opened a rich field of interplay between magnetic cooperative phenomena and semiconducting properties [1]. Diluted magnetic semiconductor (DMS) becomes a hot topic for researchers. DMS is a family of materials where it encompasses standard semiconductors, in which a sizable portion of the atoms are substituted by elements that produce magnetic moments (magnetic atoms) in a semiconductor matrix [2]. The realization of this kind of material will enable new functions in new devices.

2.1 Mechanisms of Ferromagnetism in DMS

A good starting point for the description of DMS is the Vonsovskii model [3] of the electronic structure in materials with localized magnetic moments. According to this model, there are two kinds of relevant electron states: (1) ordinary conduction and valence bands built primarily of outer s and p orbital of constituting atoms, and (2) highly localized states derived from open *d* shells of transition metals. The most distinctive feature of DMS is the strong exchange interaction between the *d* spins of the magnetic transition metal ions and the *s*, *p* carriers. In spite of this enormous activity of research, there is no current consensus on the basic magnetic model underlying the ferromagnetism of DMS. However two basic approaches to understanding the magnetic properties of dilute

magnetic semiconductors have emerged [4]. The most famous models include the Zener model of carrier-mediated ferromagnetism [5] and the Ruderman-Kittel-Kasuya-Yosida (RKKY) model [6]. These two models are similar in the sense that they all talk about the mechanism of carrier mediated ferromagnetism.

Zener [5, 7] first proposed the model of ferromagnetism driven by the exchange interaction between carriers and localized spins. Zener proposes that the spin of an incomplete *d* shell is strongly coupled to the spin of the conduction electrons. It is only when this indirect coupling, which aligns the spins in a ferromagnetic manner, dominates over the direct coupling between adjacent *d* shells that ferromagnetism is possible. The assumption that the theories make is that DMS is an approximately random alloy. However, this model was later abandoned, as neither the itinerant character of the magnetic electrons nor the quantum (Friedel) oscillations of the electron spin polarization around the localized spins were taken into account, both of these are now established to be critical ingredients for the theory of magnetic metals. In particular, a resulting competition between ferromagnetic and anti-ferromagnetic interactions leads rather to a spin glass than to a ferromagnetic ground state. In the case of semiconductors, however, the mean distance between the carriers is usually much greater than that between the spins. Under such conditions, the exchange interaction mediated by the carriers is ferromagnetic for most of the spin pairs, which reduces the tendency towards spin-glass freezing [8]. Actually, for a random distribution of the localized spins, the mean-field value of the Curie temperature T_c deduced from the Zener model is equal to that obtained

from the RKKY approach, in which the presence of the Friedel oscillations is explicitly taken into account [9, 10].

The RKKY interaction is carrier-induced, sufficiently long range to account for the magnetic interaction in dilute systems, and has been put forward to explain the carrier (hole)-induced ferromagnetism observed in a IV-VI compound PdSnMnTe [11]. A mean field theory was also developed taking into account the feed-back mechanism between the magnetization polarization and the carrier polarization; magnetization polarization produces carrier polarization and it in turn produces magnetization polarization [12]. Since the mean field theory results in the same expression of T_c as that of the RKKY interaction, it is not necessary to distinguish between the two in terms of uniform polarization of magnetization. The T_c calculated from the RKKY interaction, using the exchange constant and the hole concentration, both determined from the magnetotransport measurements, with mean free path as the cut-off length of the RKKY interaction was shown to be in good agreement with the experimentally obtained T_c [13].

A review is given on the effects of the RKKY interaction between localized spins in various dimensionality systems of doped II-VI material-based DMS [14]. Since this interaction is long-range, its influence on the temperature and magnetic field dependencies of magnetization and spin splitting of the bands is evaluated in the mean-field approximation, but by taking into considerations disorder-modified carrier–carrier interactions. The results show that the hole densities, which can presently be achieved, are sufficiently high to drive a paramagnetic–ferromagnetic phase transition in bulk and

modulation-doped structures of II–VI DMS. This strongly supports that the ferromagnetism can be controlled through changing the hole density.

2.2 Spin interactions between magnetic ions

As mentioned previously, the strong exchange interaction between the d spins of the magnetic transition metal ions and the *s*, *p* carriers is the origin of the ferromagnetism inside DMSs. We need to study the interactions that couple the spins of magnetic ions when looking for DMS with desired magnetic properties, e.g. ferromagnetism. There are several microscopic mechanisms that lead to the spin–spin (*d–d*) interactions between two magnetic ions. Two main mechanisms leading are presented in this section in the form in which they explain the interactions between magnetic ions in DMS. The two mechanisms are namely super-exchange and the double exchange.

Within the standard atomic picture, the interaction can be thought of in terms of a virtual transition between the ions and neighboring anions [4]. It has been shown that for the proper description of spin–spin interactions in semiconductors the band picture rather than the atomic one has to be used. Larson *et al*. [15] have shown that for Group II–VI DMS the dominant spin–spin interaction responsible for the magnetic behavior comes from the super-exchange.

A given magnetic ion, as a result of the *s, p–d* exchange interaction, will either be attracted or repulsed by the electrons residing in the *s, p* bands depending on their spin

orientation. This results in a spatial separation of spin-down and spin-up electrons if the bands are entirely occupied, as in insulators or intrinsic semiconductors. The super-exchange is a mechanism in which the spins of two ions are correlated due to the spin-dependent exchange interaction between each of the two ions and the *s, p* band. Such a separation clearly leads to an anti-ferromagnetic interaction between neighboring localized spins. Indeed, in the absence of holes, localized spins are anti-ferromagnetically coupled as observed in Mn-based II–VI [16] DMSs. Table 2-1 shows the filling of one-electron d orbitals and low energy orbital states for transition-metal ions in a tetrahedral environment (intermediate crystal field).

Table 2-1. Filling of one-electron d orbitals and low energy orbital states for transition-metal ions in a tetrahedral environment (intermediate crystal field)[16]

d^1 (Sc^{2+})	d^2 (Ti^{2+})	d^3 (V^{2+})	d^4 (Cr^{2+})	d^5 (Mn^{2+})	d^6 (Fe^{2+})	d^7 (Co^{2+})	d^8 (Ni^{2+})	d^9 (Cu^{2+})
Filling of one-electron orbitals								
t_{2g} -----	---------	-↑-------	-↑-↑----	-↑-↑-↑-	-↑-↑-↑-	-↑-↑-↑-	-↑↓↑-↑	↑↓↑↓↑
e_g -↑---	-↑-↑----	-↑-↑----	-↑-↑----	-↑-↑---	-↑-↑↓--	-↑↓↑↓-	-↑↓↑↓-	-↑↓↑↓-
Ground term of free ion								
^2D	^3F	^4F	^5D	^6S	^5D	^4F	^3F	^2D
Many-electron states in tetrahedral crystal field								
	-------T_1	------A_2				-------T_1	------A_2	
		-------T_2	--------E		-------T_2		-------T_2	
-------T_2				------A_1				--------E
--------E	-------T_2		-------T_2		--------E	-------T_2		-------T_2
	------A_2	-------T_1				------A_2	-------T_1	

The other mechanism of spin-dependent interaction between magnetic ions in DMS is the double exchange mechanism. This mechanism was proposed by Zener [17] in the 1950s. The double exchange couples magnetic ions in different charge states by virtual hopping of the 'extra' electron from one ion to the other. This mechanism was used to explain the magnetic properties of Mn^{2+} in II-VI DMS structures [18]. These authors considered an

Mn^{2+}–Mn^{3+} pair of ions with one d electron hopping virtually from one ion to the other via the p orbitals of neighbouring anions. The DMS with the above property are not uncommon: the best-studied examples are the Fe^{2+}–Fe^{3+} ion pairs with zero-gap II–VI compounds (HgSe and HgS) (see [19, 20] and the references therein for more information).

It has been shown in two publications [21, 22] that in a model d^4–d^5 pair of ions (Mn^{2+}–Mn^{3+} or Cr^{1+}–Cr^{2+}) in a semiconductor zinc-blend crystal, both the double exchange and the super-exchange may be effective.

2.3 Ferromagnetism in Cr doped II-VI Based DMS

In the Cr doped II-VI based DMS system, Cr doping does not introduce holes inside the semiconductor, so that the hole concentration has to be introduced through a different doping. Therefore, the magnetic property and the semiconducting property can be separately controlled through Cr doping and hole doping, respectively. In Mn-doped DMS, Mn doping also introduces holes inside the materials. So the change of Mn concentration will affect both the magnetic and semiconducting property. This is one of the reasons why there is a great interest in Cr doped II-VI based DMSs.

Owing to short-range super-exchange interactions, the Mn ion-ion spin interaction is merely anti-ferromagnetic in II-VI DMS materials. However, a net ferromagnetic super-exchange was predicted for Cr- II-VI DMS [23]. In that paper, the authors have shown

that super-exchange between two nearest-neighbor Cr^{2+} ions is dominated by the isotropic Heisenberg-type interaction, and these Heisenberg-type interactions turn out to be ferromagnetic in all the materials considered, in contrast to the case of Mn^{2+}, Fe^{2+}, and Co^{2+} studied so far. Also they have shown theoretically that Cr-based DMS are not anti-ferromagnetic and expect the above results for Cr^{2+} ions to be valid in other II-VI compounds. More recent theoretical computations have suggested that the double exchange rather than the superexchange is responsible for the ferromagnetism in Cr-based DMS [24]. In that paper, the authors used the first principle approach and the theory that DMS is a disordered system, i.e., host atoms are randomly substituted by magnetic ions, for their computations. From analyzing the present first principles calculations, the simple empirical rule is used to explain the general trends of the magnetic states of II–VI and III–V DMS. Using the rule, the authors explain that the ferromagnetism is a consequence of a delicate contest between the ferromagnetic double-exchange interaction and the anti-ferromagnetic super-exchange interaction, and its stabilization is owed to the double-exchange mechanism.

Reference:

[1] T. Kasuya, A. Yanase, Rev. Mod. Phys. **40**, 684 (1968).

[2] Tomasz Dietl and H. Ohno, MRS Bulletin (October), 714, (2003).

[3] S.V. Vonsovskii, Magnetism, John Wiley & Sons: New York, 1974.

[4] P Kacman, Semicond. Sci. Technol. **16**, R25–R39 (2001).

[5] C. Zener, Phys. Rev. **81**, 440 (1950).

[6] K. Yosida, Theory of Magnetism, Berlin: Springer, 1996.

[7] C. Zener, Phys. Rev. **83**, 299 (1950).

[8] T. Dietl, H. Ohno, Physica E **9**, 185 (2001).

[9] T. Dietl, A. Haury, Y. Merle d'Aubigne, Phys. Rev. B **55,** R3347 (1997).

[10] T. Dietl, J. Cibert, D. Ferrand, Y. Merle d' Aubigne, Mater. Sci. Eng. B **63**, 103 (1999).

[11] H. Ohno, Science **281**, 951 (1998).

[12] T. Dietl, A. Haury, Y. Merle d' Aubigne, Phys. Rev. B **55**, R3347 (1997).

[13] F. Matsukura, H. Ohno, A. Shen, Y. Sugawara, Phys. Rev. B **57**, R2037 (1998).

[14] Y. Merle d'Aubigné, A. Arnoult, J. Cibert, T. Dietl, A. Haury, P. Kossacki, S. Tatarenko and A. Wasiela, Physica E **3** (1-3), 169 (1998).

[15] Larson B E, Hass K C, Ehrenreich H and Carlsson A E , Phys. Rev. B **37**, 4137, (1988).

[16] T. Dietl, Materials, Properties and Preparations, Handbook on Semiconductors, Vol. 3B, pp1251, New York: North-Holland, 1992-1994.

[17] Zener C Phys. Rev. **82**, 403 (1951).

[18] Anderson P W and Hasegawa H, Phys. Rev. **100**, 675 (1955).

[19] Wilamowski Z , Acta Phys. Polon. A **77**, 133 (1990).

[20] Dobrowolski W, Acta Phys. Polon. A. **89**, 3 (1996).

[21] Blinowski J and Kacman P ,Acta Phys. Polon. **90**, 731 (1996).

[22] Blinowski J, Kacman P and Majewski J A, High Magnetic Fields in Physics of Semiconductors vol **2**, p861, *ed.* G Landwehr and W Ossau, Singapore: World Scientific, 1997.

[23] J. Blinowski, P. Kacman, J.A. Majewski, Phys. Rev. B **53**, 9524 (1996).

[24] K. Sato and H. Katayama-Yoshida, Semicond.Sci. Technol. **17**, 367 (2002).

Chapter 3: Molecular Beam Epitaxy (MBE) Growth Technique

3.1 MBE System

The epitaxy fabrication process was invented in 1960 by J.J. Kleimack, H.H. Loar, I.M. Ross and H.C. Theuerer [1]. In the early 1970s, demand increased for high qulity multilayered sandwiched semiconductor-insulator wafers, and A.Y. Cho developed the MBE technique to meet this need [2-4].

Molecular beam epitaxy is a technique for epitaxial growth via the interaction, which occurs on the surface of a heated crystalline substrate, of one or several molecular or atomic beams. MBE is capable of producing very thin monolayers with a precise composition at temperatures lower than those required for MOCVD (600 - 800°C). A distinguishing feature of MBE is its requirement for an ultra-high vacuum environment that on the one hand increases the technological complexity of handling the system, but also provides the advantage of *in situ* characterization of the growing material. In the industry, MBE growth method is used to fabricate the devices that produce lasers in CD players and pen-sized laser pointers.

In MBE, the constituent elements of a semiconductor are deposited onto a heated crystalline substrate in the form of ‘molecular beams’ to form thin epitaxial layers. The ‘molecular beams’ are typically from several different sources, depending on the nature of the epitaxial process. The ultra-high vacuum environment together with pure material

sources are used to obtain high-purity layers. Growth rate calibration and surface characterization are other important features to take note in MBE.

3.1.1 Main System Description [5]

This section describes the ULVAC (model: MBC-1000-2C) solid-source molecular-beam epitaxy system used in the growth process. Similar to other models of MBE systems, the ULVAC system has a preparation chamber and a growth chamber; each of them is connected with a turbomolecular pump and a rotary pump. The growth chamber is connected to a titanium getter pump (TGP) and a sputter ion pump (IP) to achieve ultra-high vacuum. The pressure in the pre-chamber can reach 10^{-5}Pa, and the pressure in the growth chamber can reach 10^{-8}Pa (with liquid nitrogen cooling the chamber's wall). Figure 3-2 shows the schematic diagram of the MBE system used in our growth. The system has seven K-cells and one valved cracker effusion cell to hold sources, and each of them has its mechanical shutter to control the on-off of the beam flux. The operation of the MBE system can be carried out through the touch-panel control board as well as computer-automation.

Figure 3-1 shows the schematic diagram of our MBE growth chamber. In this growth chamber, the substrate is placed in a special holder, which faces the K-cells. There is a heater behind the holder, so that the substrate's temperature can be held at a value necessary to obtain epitaxial growth. The crystal structure of the growing film is simultaneously checked by Reflection High Energy Diffraction (RHEED). The electron

gun reaches the surface of the film at a grazing angle, and the diffraction pattern can be observed on the RHEED screen. From the RHEED pattern showing on the screen, the quality of the growth can be observed *in-situ*.

The substrate temperature is measured by a thermocouple located at the centre of the substrate heater. However the shown temperature may not be the accurate substrate temperature since the thermocouple is at a distance from the substrate. Pyrometry is another method to determine the substrate temperature conveniently and accurately. The pyrometer is an infrared thermometer that detects directly the radiation from the surface of the substrate. However, the pyrometer's range is limited to measure between 500^{o}C and 900 ^{o}C. A pyrometer cannot be used for transparent substrates such as MgO and sapphire, which are placed on the hollow substrate holder, because the strong radiation of the heaters will transmit through the substrate and enter the pyrometer, and this will render the pyrometer's detection to be over-ranged.

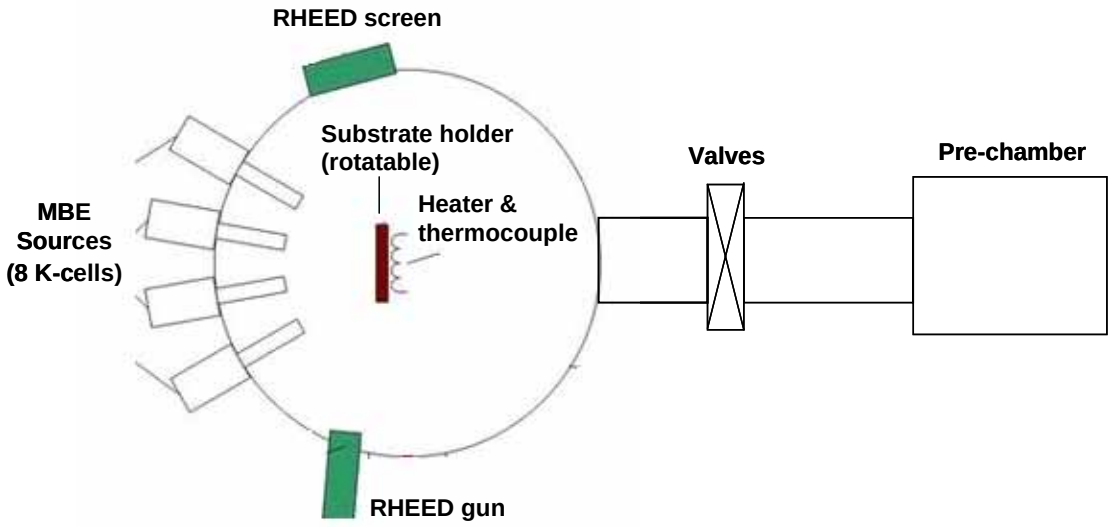

Fig 3-1. Schematic diagram of our MBE growth chamber.

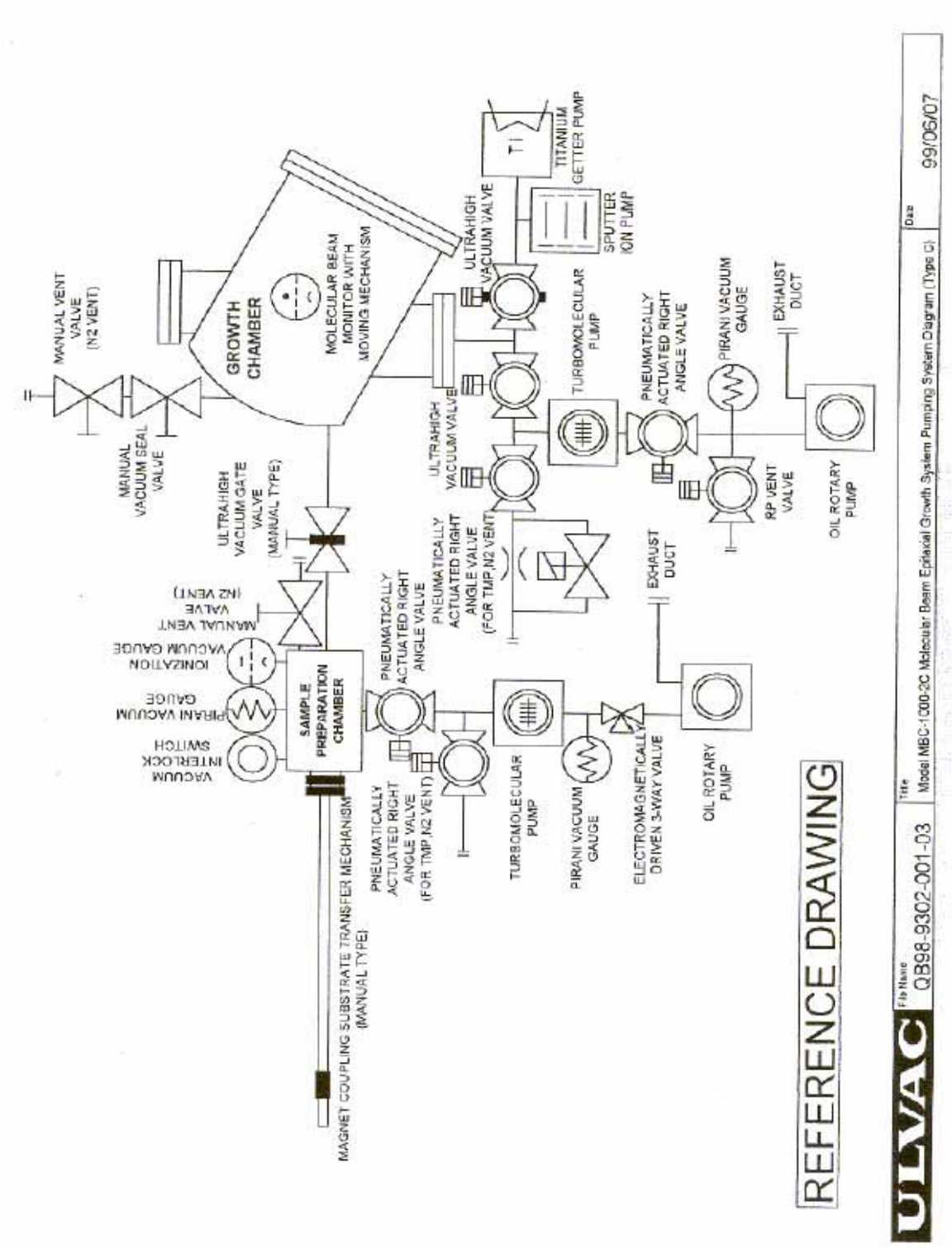

Fig 3-2. Schematic diagram of the ULVAC MBE System.

3.1.2 Knudsen Effusion Source Cells

In MBE, the constituent elements of a semiconductor are deposited onto a heated crystalline substrate in the form of 'molecular beams' to form thin epitaxial layers. The 'molecular beams' are typically from thermally evaporated elemental sources, but other sources include group II precursors (MOMBE), group VI hydride or organic precursors (gas-source MBE), or some combination (chemical beam epitaxy or CBE). To obtain high-purity layers, it is critical that the material sources be extremely pure and that the entire process be done in an ultra-high vacuum environment. Another important feature is that growth rates are typically on the order of a few Å/s and the beams can be shuttered in a fraction of a second, allowing for nearly atomically abrupt transitions from one material to another [6]. The solid source materials in this case, Cr and Zn, are held in an inert crucible which is heated by radiation from a resistance heater source and a thermocouple is used to provide temperature feedback [7]. In our MBE system, beside Cr and Zn K-cells, the other five K-cells contain Be, Mn, Ge, Mg and Co solid source.

3.1.3 Valved Cracker Effusion Cell

Unlike other sources such as Zn and Cr that use K-Cells, valved cracker effusion cell was used for tellurium (Te) source. The valved cracker used in our system is EPI-500V-S as shown in Fig 3-3. The reason for using a valved cracker is that cracked tellurium molecules are likely to have higher sticking coefficients than those of the uncracked counterparts. More importantly, the use of a cracker provides good controllability and

reproducibility of the flux in controlling the composition of tellurium containing compounds [8]. The Te source in the EPI valved cracker can be controlled manually via a micrometer valve actuator or automated by a servo motor controller (SMC). In the normal situation, the idling temperature of the cracker zone is maintained at 300^{o}C, and the temperature of the bulk crucible is maintained at 150^{o}C. During growth, the temperature of the bulk zone and cracker zone is raised to the desired values. The tellurium particles are split into tellurium molecules when they pass through the cracker zone to the growth chamber.

In our growth, we chose 650^{o}C as the cracker zone's temperature. The valved cracker uses its own DC power supply. The valved cracker has its own water-cooling system, which helps the crucible to maintain at a stable temperature. Because of the complexity of the cracker zone's structure, the valved cracker has much more surface area than conventional effusion cells. Therefore, the pumping down and outgassing process requires more time, and should be carefully attended.

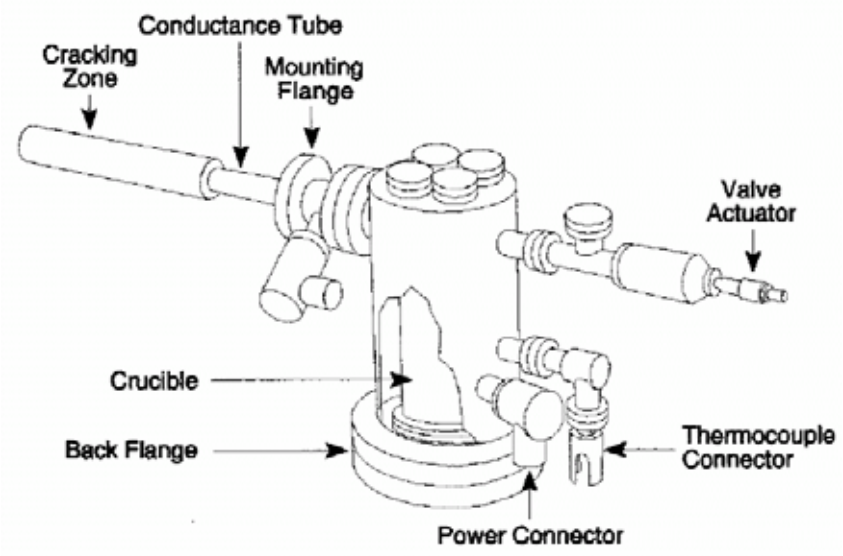

Fig 3-3. Overview of EPI-500V-S valved cracker cell.

3.1.4 Reflection-high Energy Electron Diffraction (RHEED)

The precision of the MBE to grow crystalline layer combinations with accurate dimensional control down to the atomic level would not be possible without adequately precise characterization techniques like reflection high energy electron diffraction (RHEED).

RHEED is a powerful technique that provides resolution on the atomic scale while at the same time being fully compatible with the crystal growth process; it is used for studying surface structures of flat surfaces as well as surface phase transitions. RHEED is sensitive to surface changes, either due to structure changes or due to adsorption. Therefore, it is widely used as an *in situ* probe to monitor the growth of thin films both in research and in industry.

A typical RHEED measurement system consists of an electron gun, a phosphor screen and image-processing hardware and software. A high energy beam (3-100keV) from the electron gun is directed at the sample surface at a grazing angle in the range of 0.5-2.5^{o}. The high energy of the electrons would result in high penetration depth. However, because of the glancing angle of incidence, only a few atomic layers are probed. This is the reason of the high surface sensitivity of RHEED. Figure 3-4 shows a typical MBE chamber with RHEED and the dotted line shows the paths of electrons.

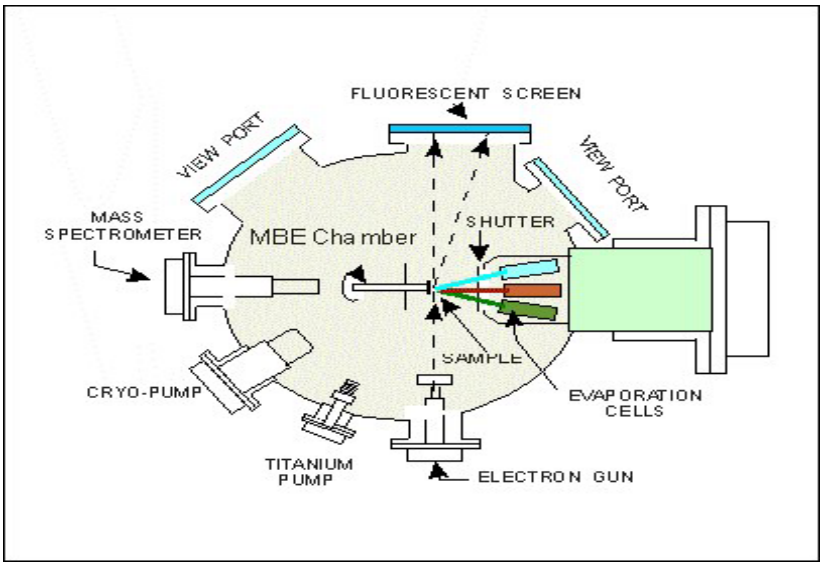

Fig 3-4. Diagram of a typical MBE system growth chamber. The dotted line shows the path of electron hitting the RHEED screen.

The electrons are diffracted by the crystal structure of the sample and then impinge on a phosphor screen mounted opposite to the electron gun. The diffraction pattern can be viewed and recorded from the atmospheric side of the window. The diffraction pattern depends on the structure and the morphology of the probed surface. The sample can be rotated about its normal axis so that the electron beam is incident along specific crystallographic directions on the surface. Figure 3-5 shows a illustration of the fundamentals of RHEED.

Despite the popularity of RHEED, there is no complete formal theory for it. However, a number of simplified kinematical approaches have been introduced that are useful for understanding the basic idea of RHEED. The simplest theory to describe RHEED is the "geometric theory"; this theory is widely used for experimental calculations. A more elaborate theory, "dynamical theory," is used for more complicated problems [9, 10].

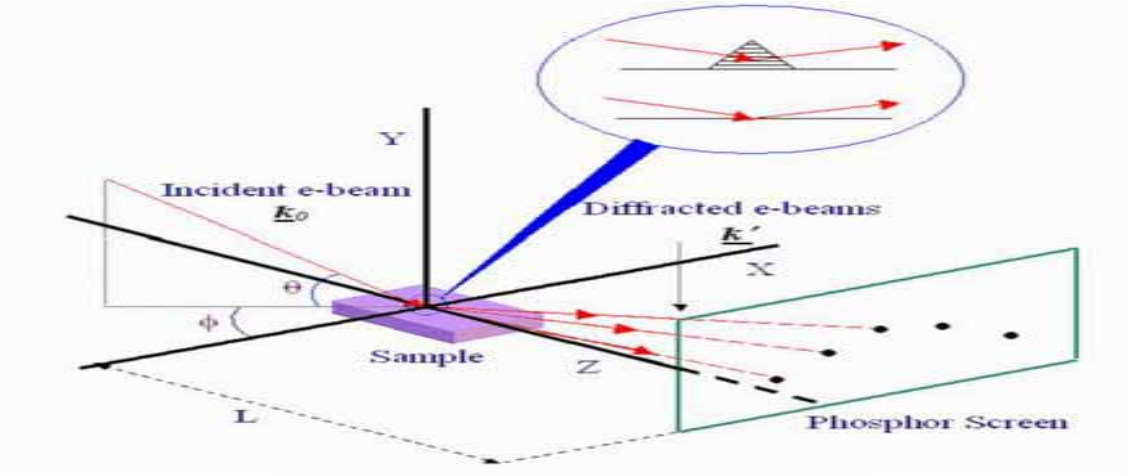

Fig 3-5. An illustration of the fundamentals of RHEED. The inset shows two kinds of reflection: transmission-reflection diffraction scattering by three-dimensional crystalline island (top) and surface scattering from flat surface (bottom) [9].

The first important information provided by RHEED patterns regards the flatness of a surface. If electrons interact only with the first atomic layer of a perfectly flat and ordered surface, the three-dimensional reciprocal lattice points degenerate into parallel infinite rods, visualized as extending infinitely in the directions perpendicular to the surface. However, in reality, due to thermal vibrations, lattice imperfections and others, diffraction from a perfectly smooth crystal surface results in a diffraction pattern consisting in a series of streaks with modulated intensity rather than points. When the surface has more than one domain (i.e., randomly oriented crystals), the RHEED image will be the sum of diffraction from all the different regions. This gives rise to a system of concentric rings. Figure 3-6 gives the different types of RHEED patterns.

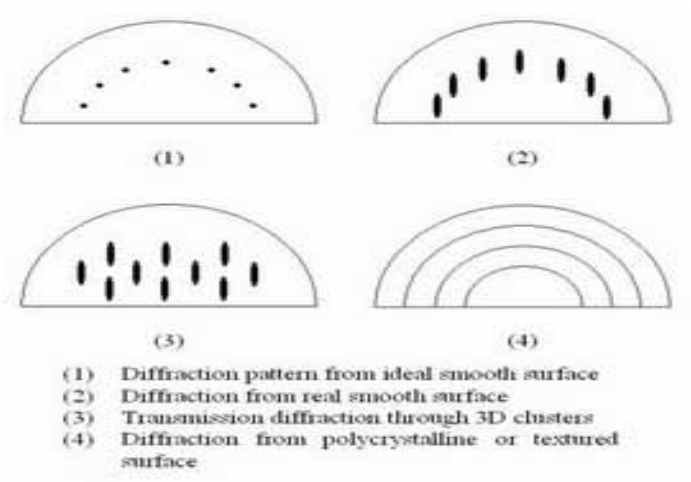

Fig 3-6. The different types of RHEED patterns.

Also, it is evident that diffraction from an amorphous surface (such as an oxide on top of a semiconductor) gives no diffraction pattern at all, and only a diffuse background will result. This is important, for example, for evaluating oxide desorption when a new substrate is initially heated up prior to growth in the MBE chamber [11].

3.2 Theoretical Background on the Epitaxy Growth Mechanism

Epitaxial growth is a process of growing film with a crystallographic relationship between film and substrate. There could be two kinds of epitaxial growth, namely homoepitaxy and heteroepitaxy. Homoepitaxy refers to the case when film and substrate are same material. Heteroepitaxy refers to the case when film and substrate are different materials. In our project, heteroepitaxy are performed. When performing heteroepitaxy, there are three possible growth modes [11]. The first, Frank-van der Merwe, is simply the successive addition of 2-D layers to the substrate crystal. The second mode, Volmer-Weber, will occur if the added material can minimize its free energy by trading increased

surface area for decreased interfacial area, forming an island structure like water droplets on glass. A third possibility can arise if the lattice spacing of the added material is a mismatch with that of the crystalline substrate. Here, growth starts with a strained 2-D wetting layer, but islands form after the first few monolayers. The driving force is the incorporation of dislocations within the islands to relieve stress. This third mode is called Stranski-Krastanow. Figure 3-7 shows clearly the three mode of growth.

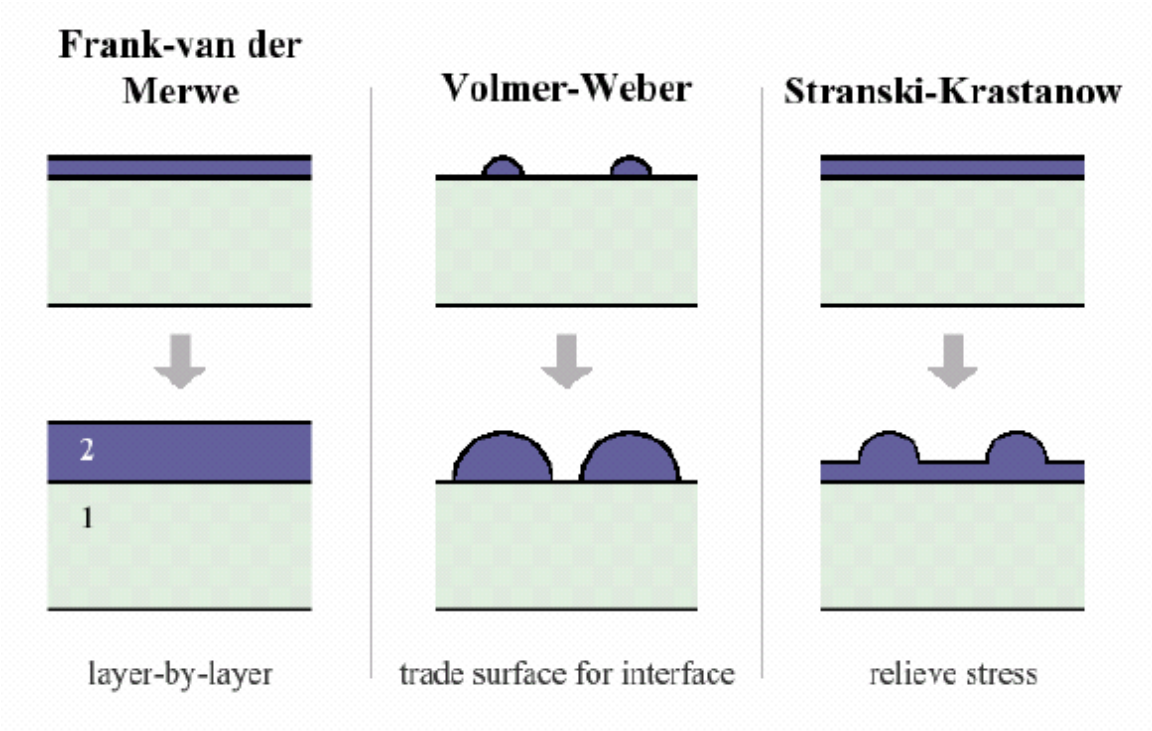

Fig 3-7. Diagram of the three growth modes.

Crystal lattice mismatch is a very important parameter in epitaxial film growth. The epitaxial growth will be affected by the mismatch ratio. The mismatch ratio can be expressed in the following form:

$$\text{Mismatch ratio } f = \frac{a_s - a_f}{a_s} \qquad (3\text{-}1)$$

where a_s is the lattice constant of the substrate and a_f is the lattice constant of the film. If the lattice constants of the substrate and film are matched, the growth will be perfect without strain, like what is shown in Fig 3-8a. If the mismatch is large, there will be mismatch dislocation [See Fig 3-8(b)]. If the mismatch is small, the film will be coherently strained [See Fig 3-8(c)]. The film will not grow following the crystal structure of the substrate. It is not epitaxial growth anymore. The limit of lattice mismatch for epitaxial growth is about 7%. If the material has a large mismatch with the substrate, a buffer layer is normally needed. The buffer layer should have better lattice match with the targeting material and also the substrate. If the buffer layer is thick enough, it can perform like a virtual substrate. Therefore epitaxial growth can be achieved even with large match between the film and the substrate.

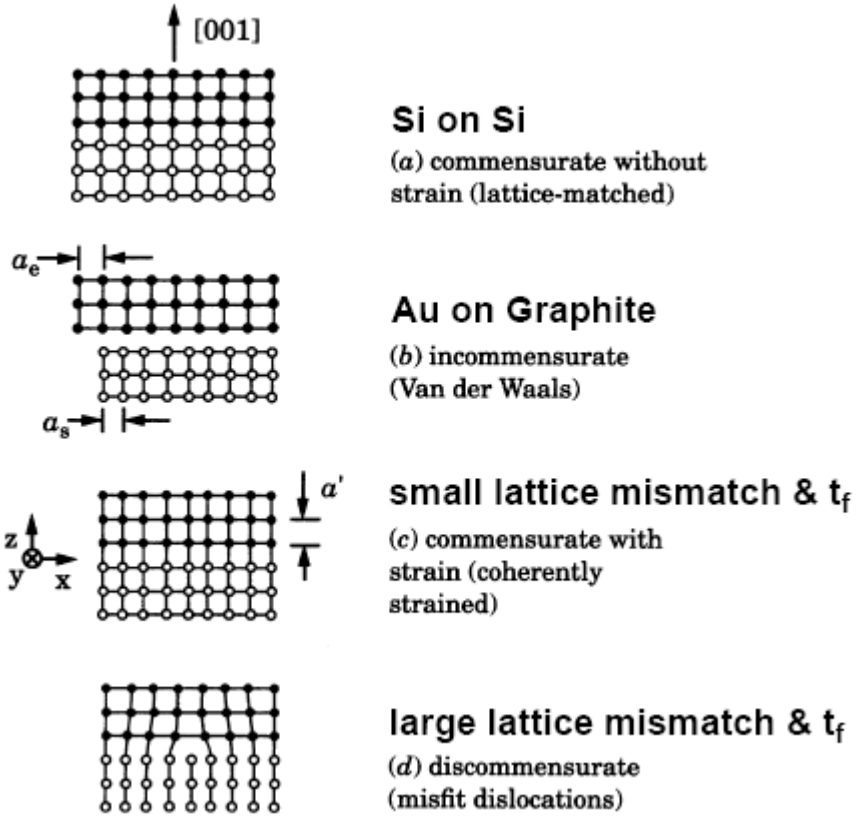

Fig 3-8. Lattice Mismatch Diagrams [15].

3.3 Growth Preparation and Procedures

3.3.1 The Use of Liquid Nitrogen to lower the Growth Chamber Pressure

As a standard procedure used in the growth by MBE, the liquid nitrogen is used to lower the pressure of the growth chamber before and during the growth because of the Cold Wall Effect [13, 14]. This procedure can lower the pressure in the growth chamber from ~10^{-8}Torr to ~10^{-10} Torr or better.

3.3.2 Temperature of the Sources

Usually the sources inside the K-cells are kept at their individual idling temperature, which is higher than the water vaporizing temperature. At that temperature, the beam equilibrium pressure (BEP) should be very low, in the order of 10^{-10} Torr. Specifically, Zn source is idling at 110^{o}C, and Cr is idling at 200^{o}C. Therefore the source will not be lost much and the source can be kept from humidity affect. Before every operation, the temperatures of the sources should be increased to their operating temperature. For tellurium source, the temperature of the bulk zone is increased to 380°C, and the cracker's temperature is increased to 650°C. Tellurium source has a BEP of about 3×10^{-7} Torr when the cracker's needle valve is opened to 100mils by the servo motor controller (SMC), and we can change the BEP by adjusting SMC.

The Cr and Zn sources' flux can be controlled by varying its effusion cells' temperature. When we did the growth, the K-cell with Cr had a typical temperature about 1250°C, this

however changes for different growths and its BEP is ~2×10^{-8} Torr. The typical BEP of Zn is ~1×10^{-6} Torr at working temperatures of ~230°C. Though we have calibrated the BEP of all sources just after loading the sources and system baking, each time before transferring the substrate into the growth chamber we should also calibrate the sources' BEP again by the flux monitor. Because the ion gauge we used in MBE is in essence a density monitor, the relative average velocities of each species must be taken into account when comparing BEP, i.e. the relative fluxes may be calculated from the relative BEP according to

$$\frac{J_x}{J_y} = \frac{P_x}{P_y} \bullet \frac{\eta_y}{\eta_x} \left(\frac{T_x M_y}{T_y M_x} \right)^{\frac{1}{2}} \qquad \text{(3-2) [16]}$$

where J_x is the flux of species x, P_x is its beam equivalent pressure, and T_x and M_x are the absolute temperature and molecular weight, respectively. η is the ionization efficiency relative to nitrogen and is given by

$$\frac{\eta}{\eta_{N_2}} = \frac{0.4Z}{14} + 0.6 \qquad \text{(3-3) [16]}$$

where Z is the atomic number. By substituting the parameters of Te and Cr into equation (3-2) and (3-3), the Te/Cr flux ratio during the growth can be found. These equations demonstrate that the flux can be controlled effectively by varying the temperature of the K-cell. Flux ratio is one of the most important parameters to adjust the growth rate and control the film quality in MBE growth.

3.3.3 Substrate Preparation

The substrate used for this project is GaAs (001) substrate, which is doped with Si. A bare substrate from the manufacturer has a diameter of 2 inches. The substrate will be cut into 1.6mm×1.6mm squares in order to fit into the substrate holder. After cutting, the substrates (normally four) will be placed inside the preparation chamber. The pre-chamber is pumped down until its pressure is close to 10^{-5} Pa. Then one of the substrates will be carried by a fork to the pre-heat area to be heated before it is sent into the growth chamber. The pre-heating is also using radiation heating method. The purpose of pre-heating is to degas and also to get rid of the water molecules sticking on the substrate. The pre-heat usually lasts for 20 to 30 minutes and the pre-heating temperature used is 300^{o}C. After pre-heating, the interlock between the pre-chamber and growth chamber is opened and the substrate holder with the substrate is transferred into the growth chamber and is placed on the manipulator, which holds the substrate holder. During substrate transferring, the manipulator is horizontal and after the transferring, manipulator is adjusted to face the K-cell. Therefore, the substrate can face the K-cells and the flux can arrive on the surface of the substrate almost perpendicularly.

3.3.4 Substrate Oxide Desorption and Thermal Annealing

The GaAs we are using is epi-ready GaAs (001) substrates. The substrate is treated with special process. There is a thin layer of oxide on the surface, which can be got rid off at certain temperature. The typical temperature for GaAs desorption is 580^{o}C [17]. Before oxide desorption, the RHEED pattern shows a haze, which is indicative of the amorphous

nature of the protective oxide. The substrate temperature is ramped up until the RHEED pattern shows streaky pattern, which denotes good crystal structure and the oxide has been removed from the surface.

After the oxide desorption, the substrate temperature is lowered to the desired growth temperature. The substrate is ready for growth.

Reference:

[1] http://www.research.att.com/history/76epit.html.

[2] A.Y.Cho, J. Appl. Phys. 41, 2780 (1970); 42, 2074 (1971); Appl. Phys. Lett. **19**, 467 (1971).

[3] A. Cho, J. Vac. Sci. Tech. **8**, S31 (1971)

[4] A. Cho, J. Arthur, Prog. Solid-State Chem. **10**, 157 (1975).

[5] ULVAC MBC-1000-2C Molecular Beam Epitaxial Growth System manual.

[6] http://www.ece.utexas.edu/projects/ece/mrc/groups/street_mbe/echapter.html.

[7] E.H.C. Parker , The Technology and Physics of Molecular Beam Epitaxy, New York : Plenum Press, 1985.

[8] F.J. Bartoli, Jr., H.F. Schaake and J.F. Schetzina, Properties of II-VI semiconductors: bulk crystals, epitaxial films, quantum well structures, and dilute magnetic systems, Pittsburgh, Pa.: Materials Research Society, 1990.

[9] http://www.hostultra.com/%7Emhegazy/rheed.htm.

[10] Wolfgang Braun , Applied RHEED- Reflection High-Energy Electron Diffraction During Crystal Growth, New York : Springer, 1999.

[11] http://www.elettra.trieste.it/experiments/beamlines/lilit/htdocs/people/luca/tesihtml/node25.html#fig:rheed1.

[12] R. J. Nichols, E. Bunge, H. Meyer and H. Baumgärtl, Surface Science **335**, 110 (1995).

[13] H. Iekda, K. Saitoh, Y. Hasegawa, A. Koukidu and H. Seki, J. Crystal Growth **115**, 211 (1991).

[14] F. Sato, T. Tatsumi, T. Hashimoto and T. Tashiro, IEEE Transactions on Electron Devices **41**, 1373 (1994).

[15] M. Ohring, The materials science of thin films, Boston: Academic Press, (1992).

[16] M. A. Herman and H. Sitter, Molecular Beam Epitaxy: Fundamentals and Current Status, New York: Springer, 1996.

[17] A.Y.Cho, J.R. Arthur, Progress in Solid State Chemistry **10**, 157 (1975).

Chapter 4: Characterization Techniques

In this project, various characterization tools were used in order to analyze the structural, compositional and magnetic properties. The basic functions of all the characterization methods used are briefly discussed here.

4.1 X-Ray Diffraction (XRD) Measurement

X-ray is generally electromagnetic radiation and it can primarily interact with electrons in atoms. The diffracted waves from different atoms can interfere with each other and the resultant intensity distribution is strongly modulated by this interaction. If the atoms are arranged in a periodic fashion, as in crystals, the diffracted waves will consist of sharp interference maxima (peaks) with the same symmetry as in the distribution of atoms. Measuring the diffraction pattern therefore allows us to deduce the distribution of atoms in a material, for example, the peaks in an X-ray diffraction pattern are directly related to the atomic distances [1]. Therefore from XRD measurement we shall be able to know most of the properties of the film related to the structure. For a given set of lattice plane with an inter-plane distance of d, the condition for a diffraction (peak) to occur can be simply written as $2d\sin\theta = n\lambda$, which is called Bragg's law after W.L. Bragg. Figure 4-1 shows the illustration of the Bragg's law.

XRD has a few functions, which can be used for thin film characterization. The two commonly used methods are lattice constants measurement and rocking-curve measurement. Through θ-2θ scans, the lattice constants could be deduced and it could

provide information about lattice mismatch between the film and substrate so that it could also indicate strain and stress. Rocking-curve is obtained by doing a θ scan at a fixed 2θ angle. The width of the rocking curve is inversely proportionally to the dislocation density in the film so that it is a gauge of the quality of the film.

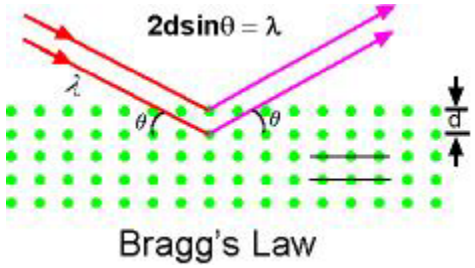

Fig 4-1. Bragg's Law demonstration [2].

4.2 Atomic Force Microscope (AFM)

An atomic force microscope (AFM) operates by measuring attractive or repulsive forces between a tip and the sample as shown in Fig 4-2. In its repulsive "contact" mode, the instrument lightly touches a tip at the end of a "cantilever" to the sample. As a raster-scan drags the tip over the sample, some sort of detection apparatus measures the vertical deflection of the cantilever, which indicates the local sample height. Thus, in contact mode the AFM measures hard-sphere repulsion forces between the tip and sample. In non-contact mode, the AFM derives topographic images from measurements of attractive forces; the tip does not touch the sample. AFM could be used for the surface characterization of the thin-films grown. Information such as surface roughness (RMS) and the surface topography is obtained from the AFM [1]. In this project, a Digital

Instruments Nanoscope III (DI-3100) multimode scanning force microscope was used for studying the topography of the films.

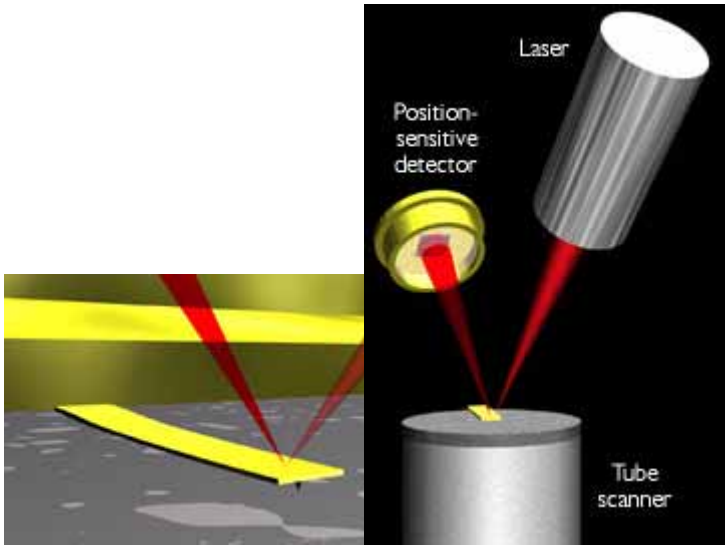

Fig 4-2. Concept of AFM and the optical lever: (left) a cantilever touching a sample; (right) the optical lever [3].

4.3 Scanning Electron Microscopy (SEM)

Scanning Electron Microscopes (SEM) are one of the most powerful and useful instruments used in nanotechnology research today. It first made its debut in 1942 and was commercially available around 1965 [5]. The SEM exhibits many advantages over the traditional light microscope. It can magnify a sample up to 300,000 times. It provides tremendous depth of field and high resolution. The images obtained from SEM are obtained in 3-dimensions. Since its development, it has found applications in a wide variety of fields and spawned new areas of study in medical and physical science communities. Figure 4-3 shows the schematic graph of a SEM system. The SEM used in this project uses field emission (FE) sources, which have the smallest beam diameter and

they can operate at much lower beam voltages while still achieving adequate spatial resolution. The purpose of the SEM is to view the surface structure of the thin films grown and compare with the images taken with the AFM.

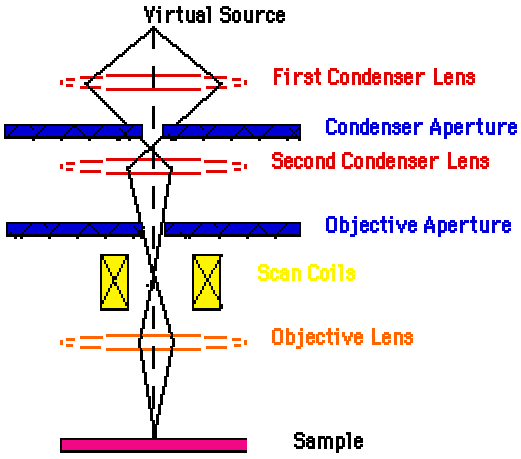

Fig 4-3. Picture of SEM-EDX system [4].

4.4 Energy Dispersive X-ray Spectrometer (EDX)

EDX is the measurement of X-rays emitted during electron bombardment in an electron microscope (SEM or TEM) to determine the chemical composition of materials on the micro and nano- scale. By determining the energies of the X-rays emitted from the area being excited by the electron beam, the elements present in the sample are determined. The rate of detection of these characteristic X-rays is used to measure the amounts of elements present (quantitative analysis). If the electron beam is rastered over an area of the sample then EDX systems can also acquire X-ray maps showing spatial variation of elements in the sample. It can detect the full range of elements from Boron (atomic no. 5) to Uranium (atomic no. 92) [1].

In our experiment, we use a JEOL JSM-6700F Field Emission Scanning Electron Microscope (SEM) with Oxford INCA Energy Dispersive X-ray (EDX) Spectrometer. The electron energy used is 15keV.

4.5 Vibrating Sample Magnetometer (VSM) Measurement

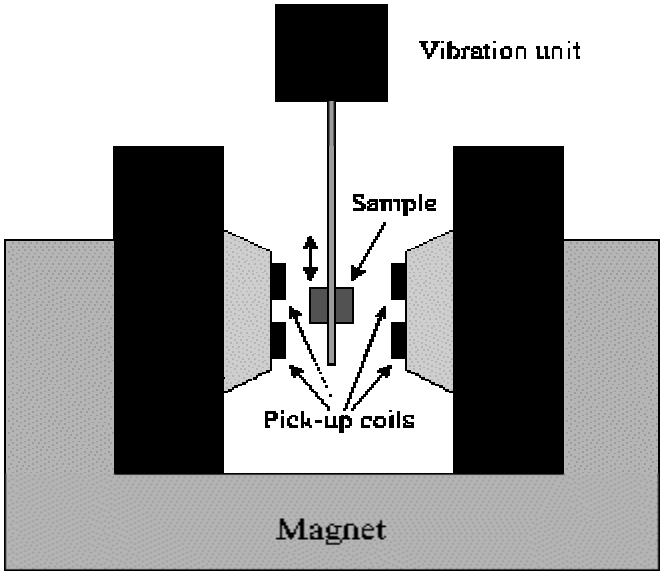

Fig 4-4. Schematic diagram of the VSM [6].

The Vibrating Sample Magnetometer (VSM) is the basic instrument for characterizing magnetic materials. Since its invention some forty years ago, it has become the workhorse in both laboratory and production environments for measuring the basic magnetic properties of materials as a function of magnetic field and temperature. The VSM is used in this project for the testing of hysteresis in II-VI magnetic materials that have been grown.

The VSM is schematically shown in Fig 4-4. In this instrument the magnetic field is controlled by an electromagnet. The electromagnet surrounds the sample and detection coils and is used for varying the field to which the sample is exposed so that the magnetization can be measured as a function of the applied field. A sample is connected through a rod (sample holder) to a vibration unit. The sample is placed in the middle of a set of pick-up coils in which the voltage will be induced. The magnetic field magnetizes the sample, which is vibrating at a relatively high frequency. The magnetized sample creates flux in the pick-up coils and voltage in the pick-up coils is induced due to changes of flux caused by the sample vibration. The sensitivity of the VSM machine in the lab is around 10^{-6} emu.

4.6 Superconducting Quantum Interference Device (SQUID) Measurement

The most sensitive device for magnetic field detection is the Superconducting Quantum Interference Device (SQUID). The device has been developed for traditional low temperature superconductors requiring cooling with liquid Helium to 4 Kelvin (-269^{o}C) and is commercially available from several suppliers. The developed SQUIDs have been characterized in terms of magnetic field sensitivity. The bare SQUID device has a typical magnetic field sensitivity of 2 pT, while for SQUIDs coupled to a superconducting input coil, 100 fT has been demonstrated [7]. Figure 7-8 shows the schematic diagram of SQUID system. In this project, a standard commercial SQUID system manufactured by Quantus was used. The temperature range used was from 5K to 400K. The magnetic field

used during measurement was up to 3T although the machine can achieve 7T maximally [5].

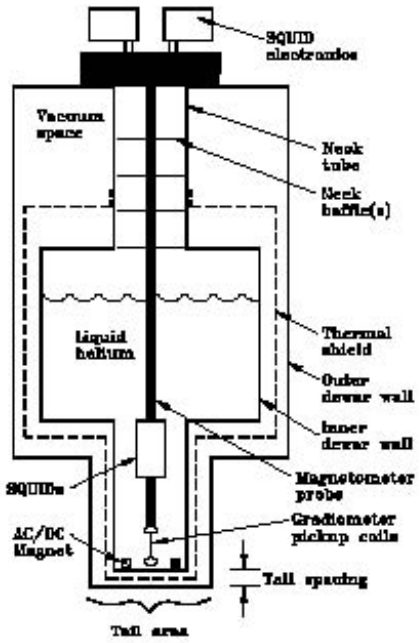

Fig 4-5. Schematic diagram of SQUID [8].

4.7 Particle Induced X-ray Emission (PIXE) measurement

Particle induced X– ray emission [PIXE] is a kind of analysis based on the measurement of the energies and intensities of characteristic X-radiation emitted by a test portion during irradiation with charged particles other than electrons. Accelerated ions, usually helium or hydrogen, are sent into a user's test sample. The moving particles impact and displace electrons within the sample. When these missing electrons are replaced within an atom, a characteristic X-ray is emitted. By catching and analyzing the X-rays, the user can identify most of the elements found in the sample [9]. Figure 4-7 shows the working principles of PIXE. By using PIXE it is possible to obtain the absolute concentrations of

the elements. In this project, we use PIXE to determine the Cr concentration of the grown Cr doped ZnTe samples.

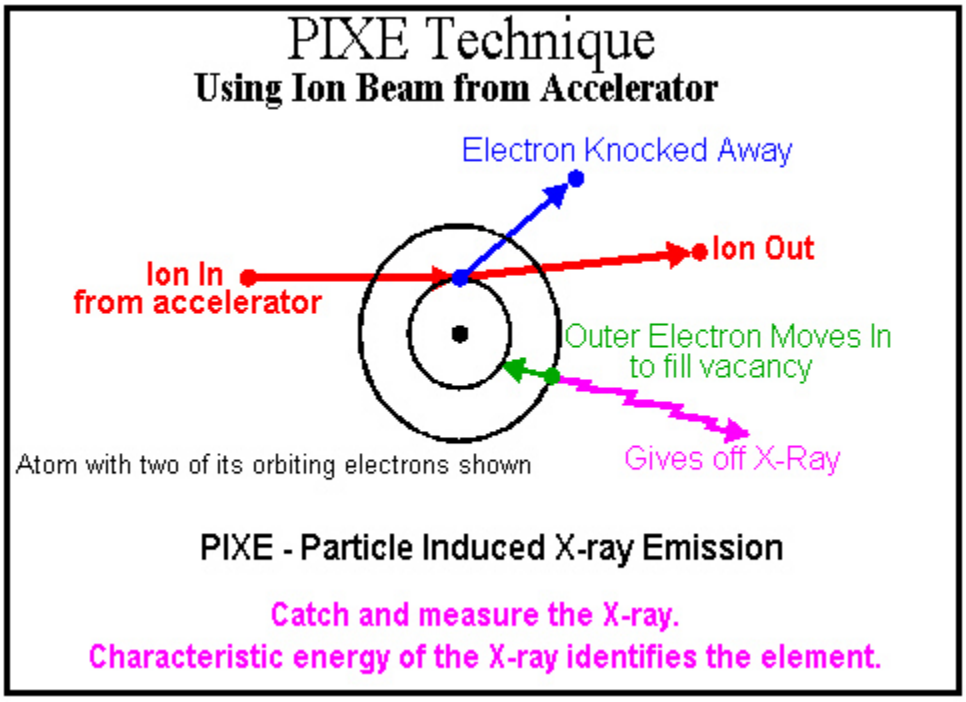

Fig 4-6. PIXE working principle [10].

Reference:

[1] L. I. Maissel and R. Glang, Handbook of Thin Film Technology, New York: McGraw-Hill, 1970.

[2] http://www.mrl.ucsb.edu/mrl/centralfacilities/xray/xray-basics/Xray-basics.html#x0

[3] http://stm2.nrl.navy.mil/how-afm/how-afm.html

[4] http://www.unl.edu/CMRAcfem/semoptic.htm

[5] Manuals for JEOL JSM-6700F Field Emission Scanning Electron Microscope (SEM) & Oxford INCA Energy Dispersive X-ray (EDX) Spectrometer

[6] Dennis Speliotis, Getting the most from your Vibrating Sample Magnetomether, ADE Techonologies, Inc., Newton, MA, USA

[7] Manual for Magnetic Property Measurement System (MPMS) sample magnetometer EverCool system.

[8] http://www.vanderbilt.edu/biomag/squid.htm

[9] Y. Strusser, C. R. Brundle and G. E. McGuire, Characterization in Silicon Processing, Boston : Butterworth-Heinemann (1993).

[10] http://ibl.albany.edu/research/techniques/pixe.html

Chapter 5: Results and Discussion

ZnTe has a zinc-blend (ZB) structure with a lattice constant of $a \sim 6.103$ Å and GaAs also has a ZB structure with $a \sim 5.654$ Å. The lattice mismatch between the two materials is 7.9%. Although the mismatch is quite large, it has been found that ZnTe could be grown quite easily on the GaAs (001) substrate. The conditions for growing stoichiomatric ZnTe films were explored first. By varying the substrate temperature and Zn to Te flux ratio, the optimum growth conditions for ZnTe were established. The appropriate substrate temperature for the growth should be between 200°C and 250°C. The Zn to Te flux ratio was established to be in the range of 1.2 to 2.7. Figure 5-1 shows the RHEED pattern of (a) GaAs after desorption and that of (b) ZnTe after 10 minutes growth. From the RHEED pattern, it can be concluded that the ZnTe film can be grown following the structure of GaAs substrate.

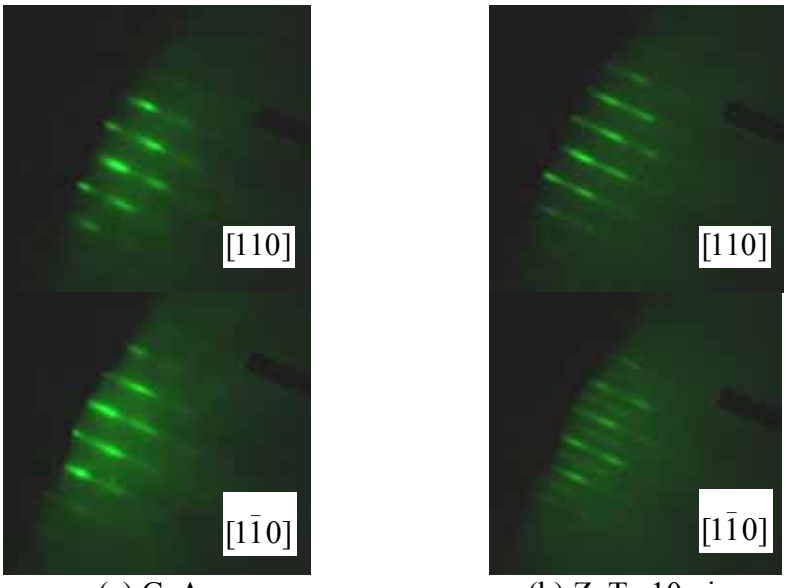

(a) GaAs (b) ZnTe 10mins

Fig 5-1. RHEED pattern of (a) GaAs desorption and (b) ZnTe after 10mins growth.

After establishing the ZnTe growth conditions, Cr molecules were introduced into the chamber together with Zn and Te molecules. The observation of RHEED pattern showed that doping of Cr reduced the crystal quality of the film. Figure 5-2 shows the time sequence of RHEED pattern in a sample grown with Cr atomic fraction $x \sim 0.14$ for [110] and $[1\bar{1}0]$ directions. Figure 5-2(a) shows the RHEED pattern after GaAs desorption. Figure 5-2(b) shows the RHEED pattern after 10 minutes ZnTe film growth. The streaky (2 × 1) RHEED pattern suggested that the ZnTe buffer layer with thickness of ~ 40nm was thick enough to act as a virtual substrate. Subsequently, we could start the growth of Cr doped ZnTe. After the shutter of the Cr cell was opened, the RHEED pattern became diffused immediately. After the growth of a few monolayers, the RHEED pattern became clearer, but less streaky compared to that of the ZnTe buffer layer [See Fig 5-2(c)]. The RHEED pattern lost its streakiness with the time of growth and became spotty [See Fig 5-2d]. When the growth continued, the RHEED pattern became more and more spotty and the spots became more diffused [See Fig 5-2(e), (f), (g), (h)]. The spotty RHEED pattern suggested that the surface of the film became rougher with the doping of Cr. The spotty pattern also indicated that the film followed the island growth mode.

In order to obtain the optimum growth conditions, a few samples were grown under different substrate temperature and different Cr/Te ratio. The dependencies of substrate temperature and of Cr/Te ratio were investigated. The results are discussed separately as follows.

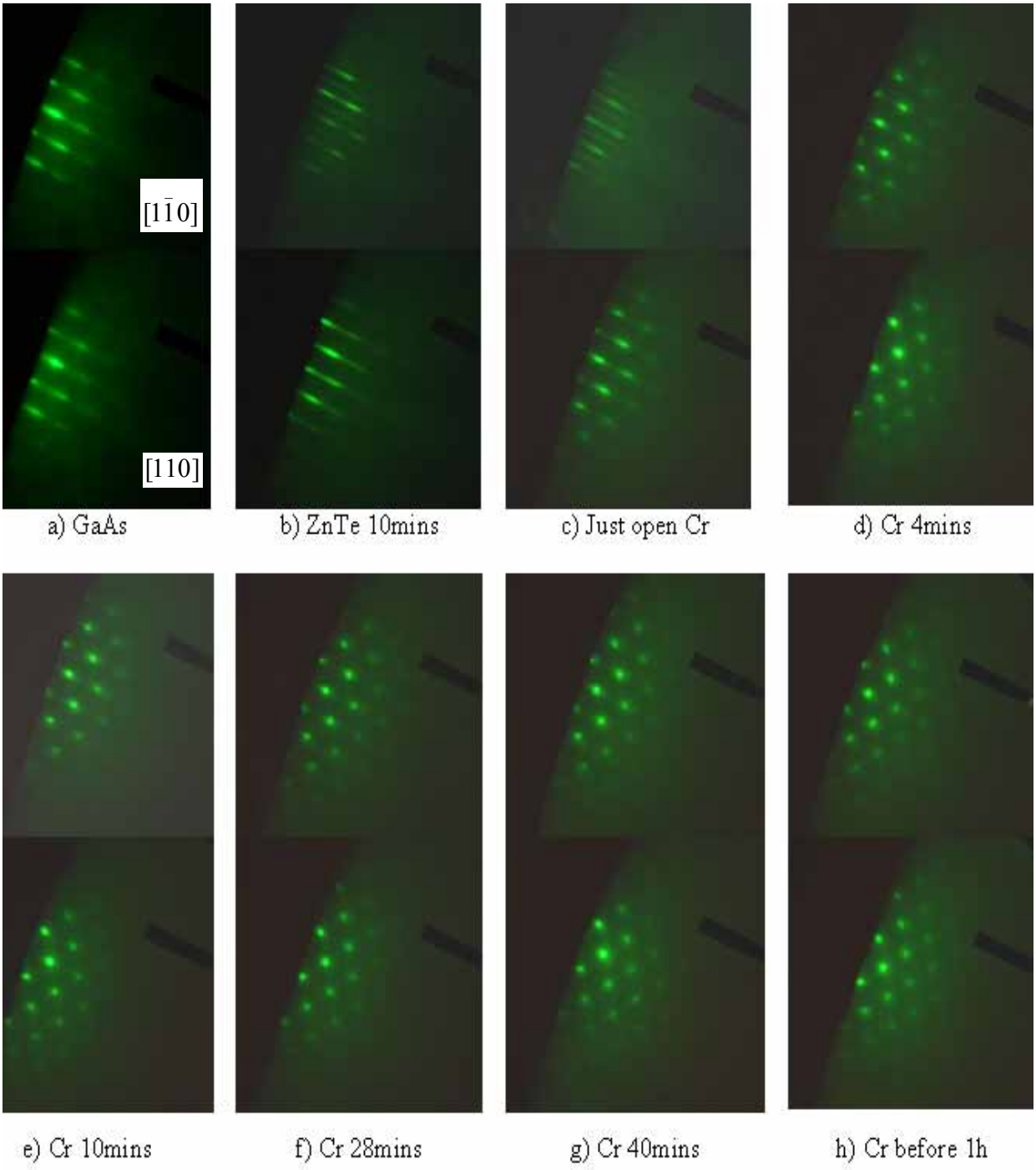

Fig 5-2. RHEED pattern for a sample growth. From (a) to (h), the upper panel were taken at direction of [1$\bar{1}$0] and the lower panel were taken at direction of [110].

5.1 Dependencies of Substrate Temperature

Substrate temperature is an important parameter, which affects the growth rate and the quality of growth. The sticking coefficient of molecules will change under different substrate temperature. The higher the temperature, the more difficult it is for the molecules to stick on the surface and the lower the growth rate will be. In this project, a few growths were done under different substrate growth temperature varying from 100^{o}C to 400^{o}C. At the same time, the Zn/Te flux ratio and Cr/Te flux ratio were kept constant for these growths. From these growths we would like to find the optimum substrate temperature for high quality growth of ZnCrTe. The Cr cell temperature was set as 1200^{o}C. The structural and magnetic characterization results for these samples are discussed in the following sections.

5.1.1 Structural Properties

RHEED pattern provides information on the quality of the growth. Figure 5-3 shows the RHEED patterns for growths at substrate temperature T_s=100^{o}C, 200^{o}C and 400^{o}C. Pictures were taken at 15 minutes after the Cr cell shutter was opened. The ZnTe buffer layers all showed streaky (2×1) RHEED patterns, which suggest that the Cr doped ZnTe layers were grown on a thick virtual ZnTe substrate. The results showed that growth at T_s ~100^{o}C and 200^{o}C had similar RHEED patterns. However, growth at T_s~200^{o}C had streakier and clearer RHEED patterns. On the other hand, growth at T_s ~ 400^{o}C showed very different RHEED patterns. The streaky lines and bright spots showed that there

might be different phases grown in the film. The RHEED patterns shown in Fig 5-3 persisted till the end of the 30 minutes growths.

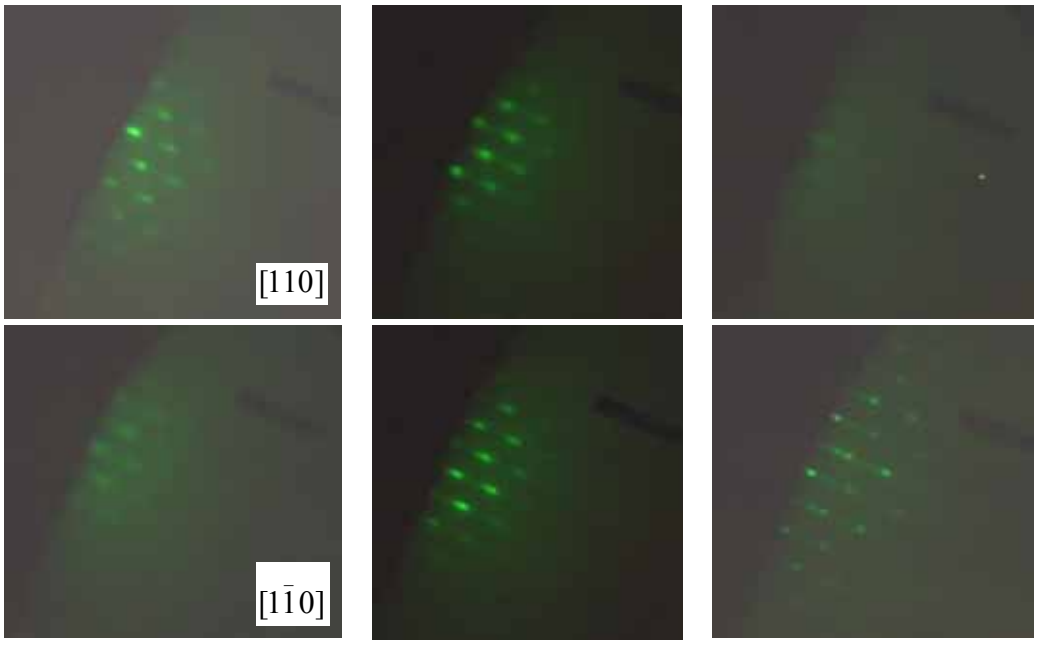

(a) 100^{o}C (b) 200^{o}C (c) 400^{o}C

Fig 5-3. RHEED pattern of Cr doped ZnTe growth in [110] and [1$\bar{1}$0] direction under substrate temperature (a) 100^{o}C, (b) 200^{o}C and (c) 400^{o}C. Pictures were taken at 15mins after Cr cell shutter was opened.

The AFM and SEM measurements showed the surface morphology, which could help us to correlate the observation of the RHEED patterns that were described previously. Figure 5-4 presents the 1μm×1μm AFM images and the corresponding SEM images. The SEM images were magnified 50,000 times. It was observed that the AFM and SEM images were similar for T_s=100^{o}C and T_s=200^{o}C samples. Small grains can be observed clearly from the AFM images for both of the samples. The SEM images also show uniformly spread grains. The root mean square (RMS) values of roughness were 2.1nm

for sample with T_s=100°C and 1.6 nm for T_s=200°C. The results were consistent to the observation of the RHEED patterns. Similar spotty RHEED pattern were observed for these two samples. However, the sample with T_s=400^{o}C shows very different AFM and SEM images. Bigger grains compared to the previous two samples were observed from both the AFM and SEM images. The grains show rectangular-like shape and it suggested big islands were grown on the surface of this film. The RMS value for this sample was 9.1nm, which confirmed that the surface of this sample was very rough. These islands observed could be responsible for the streaky RHEED pattern with bright spots [See Fig 5-3]. The 3-D image of AFM scanning [See Fig 5-5] further confirmed that the sample with T_s=200^{o}C had the flattest surface and the sample with T_s=400^{o}C had worst surface flatness among the three samples. Therefore we could conclude that T_s=200^{o}C could be the more appropriate substrate temperature for Cr doped ZnTe growth.

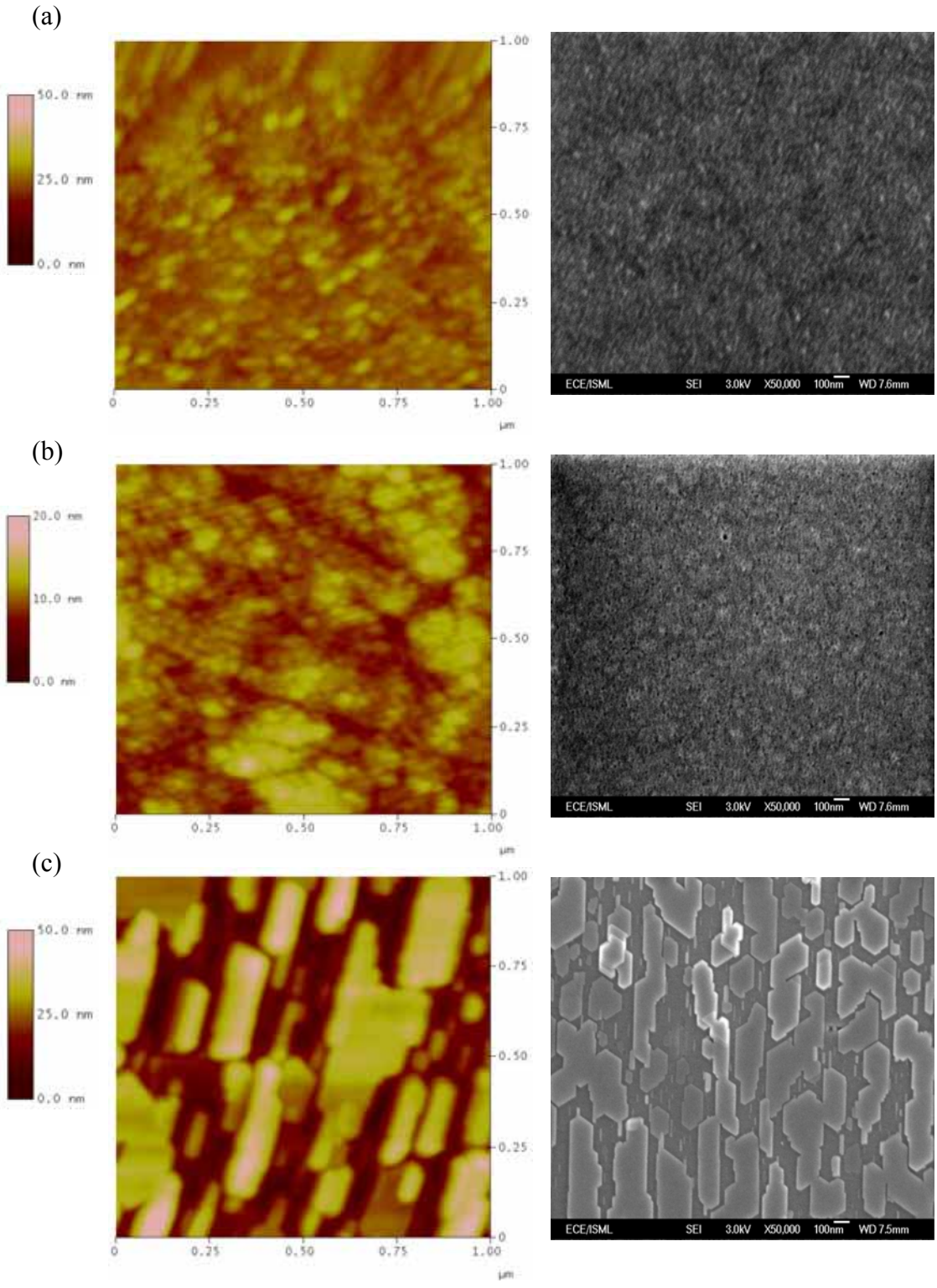

Fig 5-4. AFM (left panel) and SEM images (right panel) of $Zn_{1-x}Cr_xTe$ film with (a) T_s=100°C, (b) T_s=200°C, (c) T_s=400°C

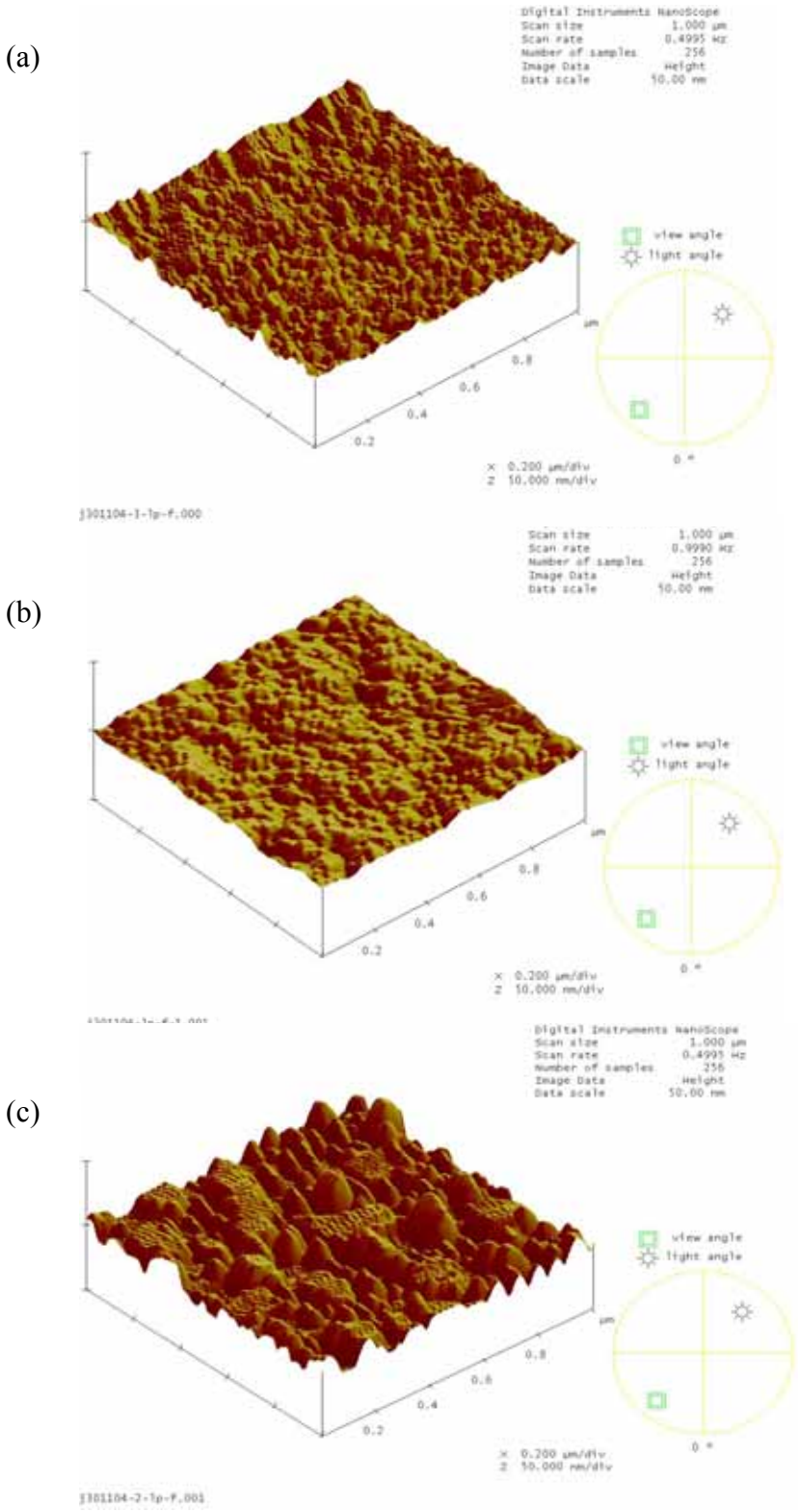

Fig 5-5. 3D topography of the $Zn_{1-x}Cr_xTe$ film (a) T_s=100°C, (b) T_s=200°C and (c) T_s=400°C.

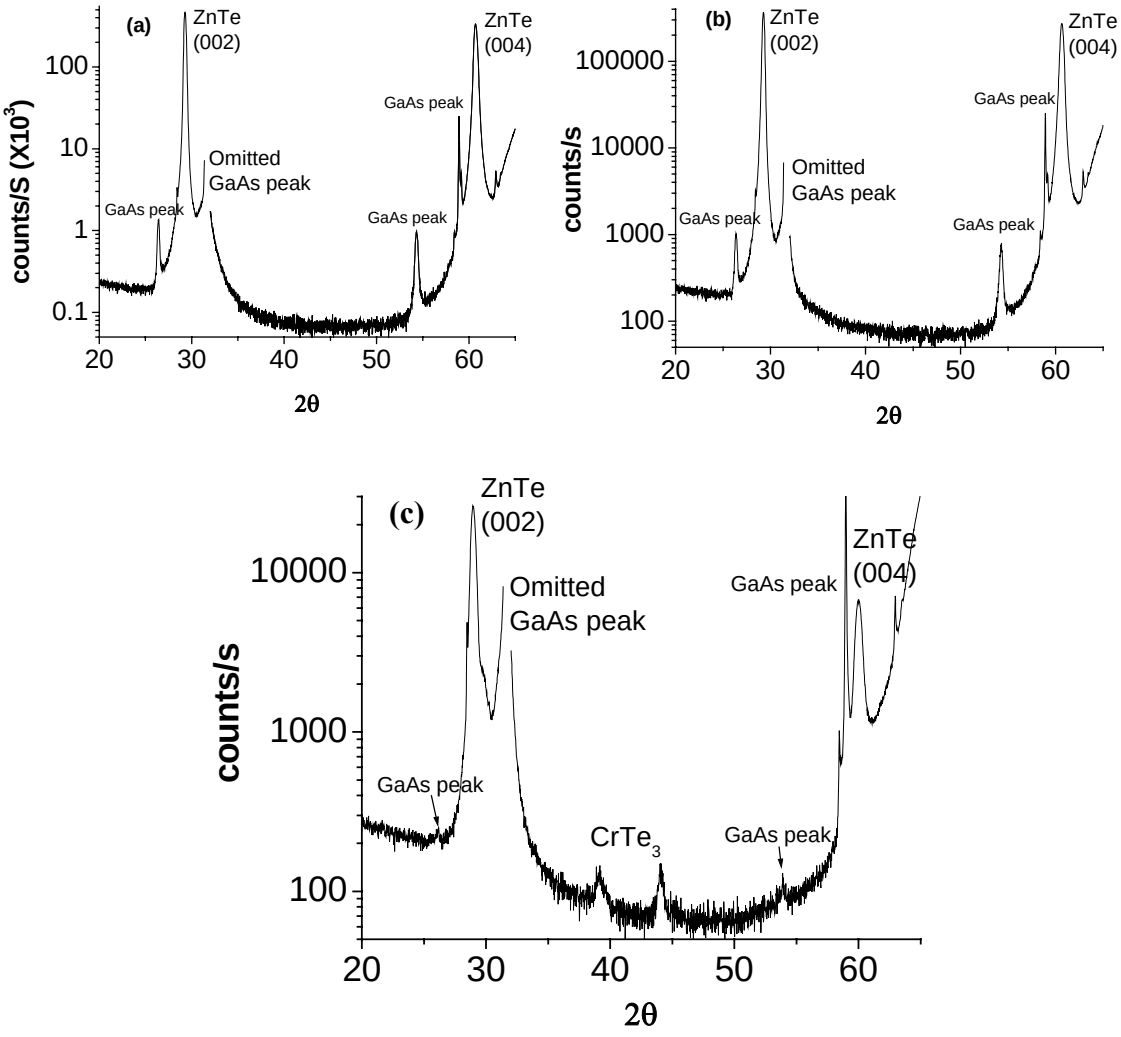

Fig 5-6. XRD θ-2θ scans for sample grown at (a) T_s=100°C, (b) T_s=200°C and (c) T_s=400°C. The Y axis is plotted in log scale. The GaAs peak refers to peaks generated by other wavelength X-ray.

The structural properties of these three samples were further analyzed by XRD. The films were scanned from 2θ of 20° to 65° and the strongest peak at 31.7° of the GaAs substrate was omitted in order to protect the detector of the XRD system. The scan results are shown in Fig 5-6 (a), (b) and (c), for samples grown at T_s =100°C, T_s =200°C and T_s = 400°C, respectively. Besides the desired 2θ peaks, some small peaks of GaAs substrate were always picked up due to the existence of X-ray with other wavelengths in the XRD

system we used. [002] and [004] peaks of ZB ZnTe could be observed clearly for samples with T_s =100^{o}C and T_s =200^{o}C. There was no other peak observed except the GaAs peaks. This suggested that there could be no other phase found for samples with T_s=100^{o}C and T_s =200^{o}C according to XRD measurements. The XRD scan result for T_s=400^{o}C showed two peaks at 39.28^o and 44.10^o, which could not be identified according to ZB ZnTe and GaAs. Through a thoroughly literature survey, we found that these two peaks' positions were very close to the XRD 2θ spectrum of monoclinic $CrTe_3$ [1]. The RHEED pattern has suggested there might be other phases grown in this sample. Therefore, we could conclude from both the results of XRD and RHEED pattern that there possibly exists monoclinic $CrTe_3$ crystal phases inside the film grown with T_s=400^{o}C.

Although we cannot totally exclude the possibility of the presence of $CrTe_3$ precipitate inside the sample grown with T_s=200^{o}C, the results of RHEED pattern, XRD scan, AFM and SEM measurements all showed that T_s=200^{o}C will be able to reduce the growth of $CrTe_3$ precipitate comparing with T_s=400^{o}C. For growth at T_s=400^{o}C, it seems that $Cr_{1-\delta}Te$ precipitates were easily formed under such a high substrate temperature. The reason could be that 400^{o}C is higher than the melting temperature of Zn (123^{o}C at 10^{-8} Torr [2]), so that it is very difficult for the Zn molecules to stick on the surface. It is easier for Cr and Te to form compounds when fewer Zn molecules are introduced on the surface. It is possible for T_s=100^{o}C to be used; however the MBE system takes a long time to reach 100^{o}C from a higher temperature. Therefore we select T_s=200^{o}C as the most appropriate substrate temperature for Cr doped ZnTe growth in this project.

5.1.2 Magnetic Properties

The effect of substrate temperature on magnetic properties was also investigated. Room temperature and low temperature (100K) VSM measurements were conducted for these three samples, which were grown at T_s=100^{o}C, T_s=200^{o}C and T_s=400^{o}C. Figure 5-7 shows the VSM measurement results at 100K. For the sample with T_s=100^{o}C, the hysteresis loop was not obvious. This sample was measured to have a T_c ~ 75k using SQUID. Thus it is beyond the detecting limit of VSM. Clear hysteresis loops were observed for both samples with T_s=200^{o}C and T_s=400^{o}C. In the previous discussion, XRD scan showed that there might be $CrTe_3$ precipitates inside the sample with T_s=400^{o}C. According to the literature, $Cr_{1-\delta}Te$ compound is ferromagnetic [3]. Therefore, the magnetization we observed in Fig 5-7(c) might come from the $CrTe_3$ precipitates. Therefore, only the sample with T_s=200^{o}C might exhibit ferromagnetic property from $Zn_{1-x}Cr_xTe$ DMS. These results suggested that less Cr might be doped inside ZnTe with T_s=100^{o}C than with T_s=200^{o}C. This also supports our decision to use T_s=200^{o}C as the most appropriate substrate temperature.

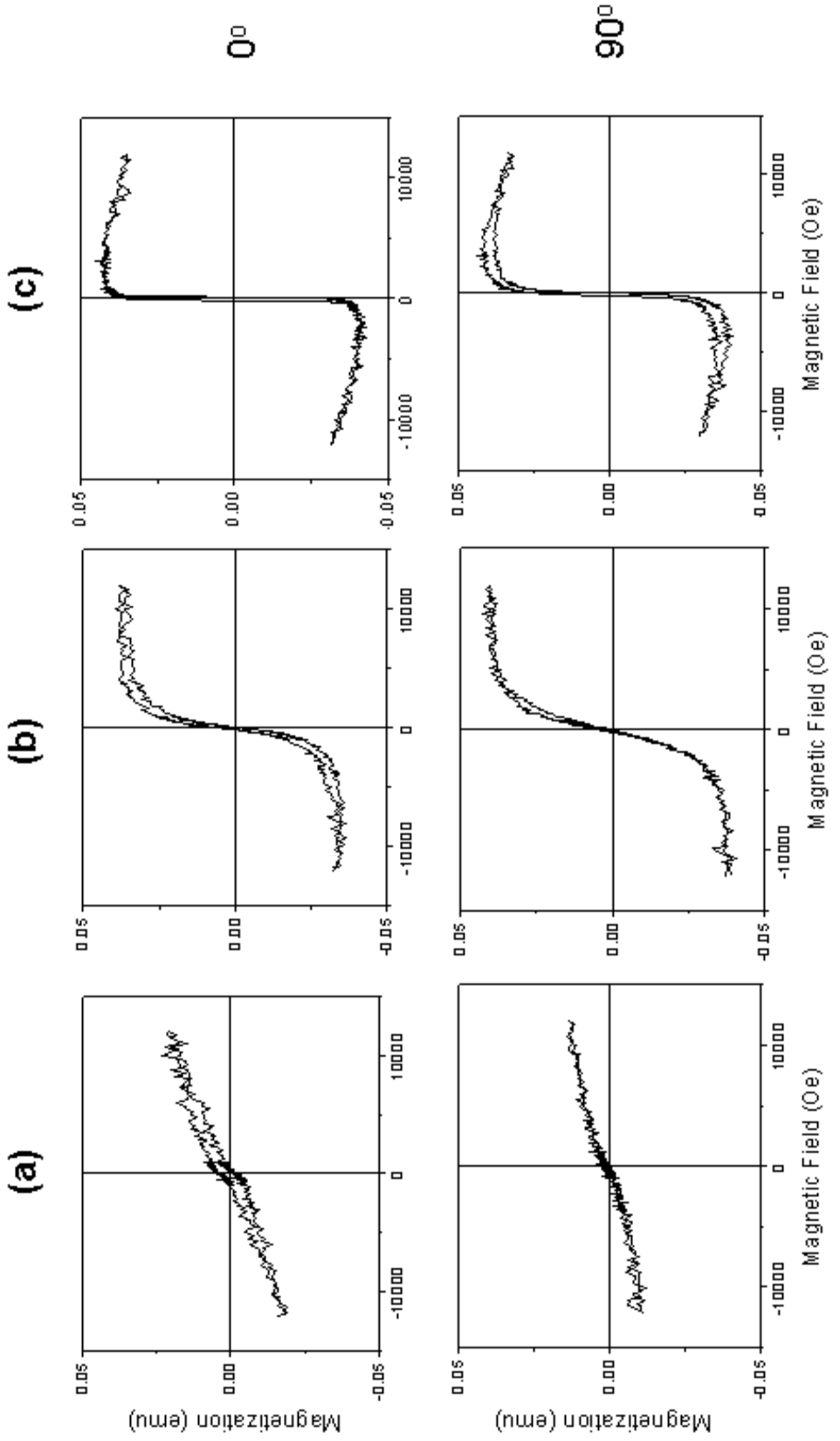

Fig 5-7. Field dependency of magnetization of ZnCrTe measured at 100k for sample with (a) T_s=100°C, (b) T_s=200°C and (c) T_s=400°C. Field was applied parallel to the sample surface. Field applied direction for the upper and lower panel were in orthogonal relationship (0^o and 90^o).

The temperature dependency of magnetization (M-T) was investigated through SQUID measurements and the results are shown in Fig 5-8. The T_c of the three samples was roughly estimated as the temperature where the magnetization disappeared. The T_c found was 75K for T_s=100^{o}C, 185K for T_s=200^{o}C and 320K for T_s=400^{o}C. The T_c for sample with T_s=400^{o}C fell into the T_c range (180K ~ 340K) for chromium tellurides precipitates provided by the literature [3], which suggested that our analysis could be correct. The M-T curve of this sample also shows some fluctuation at temperature lower than ~120K. This suggested that there could be different magnetic phases inside this sample. The T_c for the sample with T_s=100^{o}C is lower than 100K. This confirms that there was no hysteresis loop detected at 100K by VSM for this sample. The T_c for the sample with T_s=200^{o}C was higher than that for the sample with T_s=100^{o}C. This indicates that T_s=200^{o}C was more promising for achieving higher T_c. In summary, the growth at T_s = 200^{o}C is a more appropriate substrate temperature for Cr-doped ZnTe thin film. Therefore all the later growths were carried out with the substrate temperature of 200^{o}C.

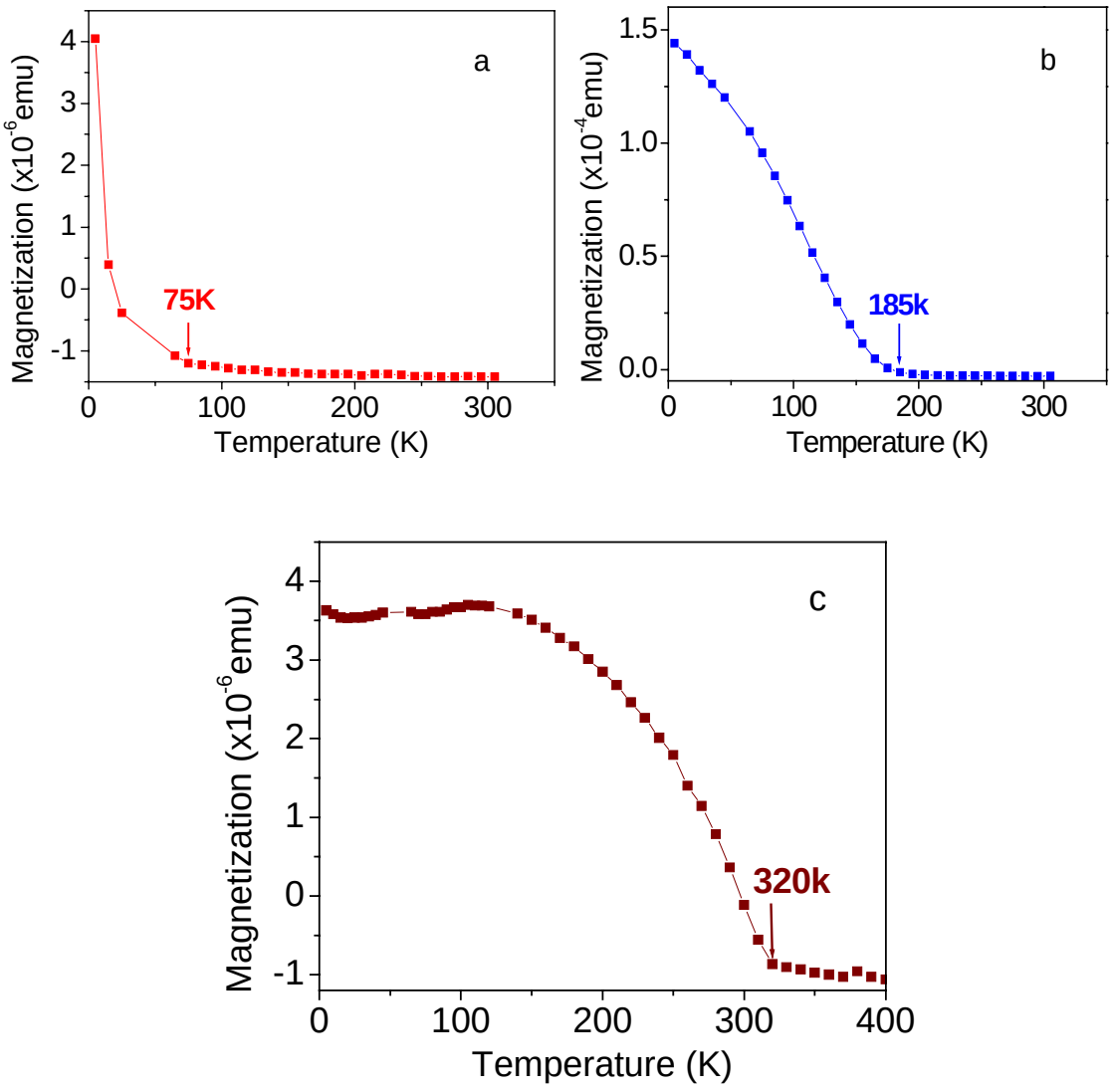

Fig 5-8. M-T measurement for samples with (a) T_s=100°C, (b) T_s=200°C and (c) T_s=400°C. 100Oe magnetic field was applied for all the measurements.

5.2 Dependencies of Cr/Te flux ratio

It was well known that the beam equilibrium pressure (BEP) was proportional to the K-cell temperature. The relationship between Cr BEP and Cr K-cell temperature was plotted in Fig 5-9. From this proportional relationship, BEP under any Cr K-cell temperature

could be estimated. Furthermore, the Cr/Te flux ratios could be calculated using eq. (3-2). Then we could obtain the nominal Cr doping concentration according to the Cr/Te and ZnTe flux ratio. The Zn/Te flux ratio was varied from 1.21 to 1.48. The nominal Cr doping concentration was calculated using eq. (5-1). The Cr/Te flux ratios and the nominal Cr doping concentrations with respect to seven different Cr K-cell temperatures were tabulated in Table 5-1.

$$\text{Nominal Cr concentration (\%)} = \frac{f(Cr/Te)}{f(Cr/Te)+f(Zn/Te)} \qquad (5\text{-}1)$$

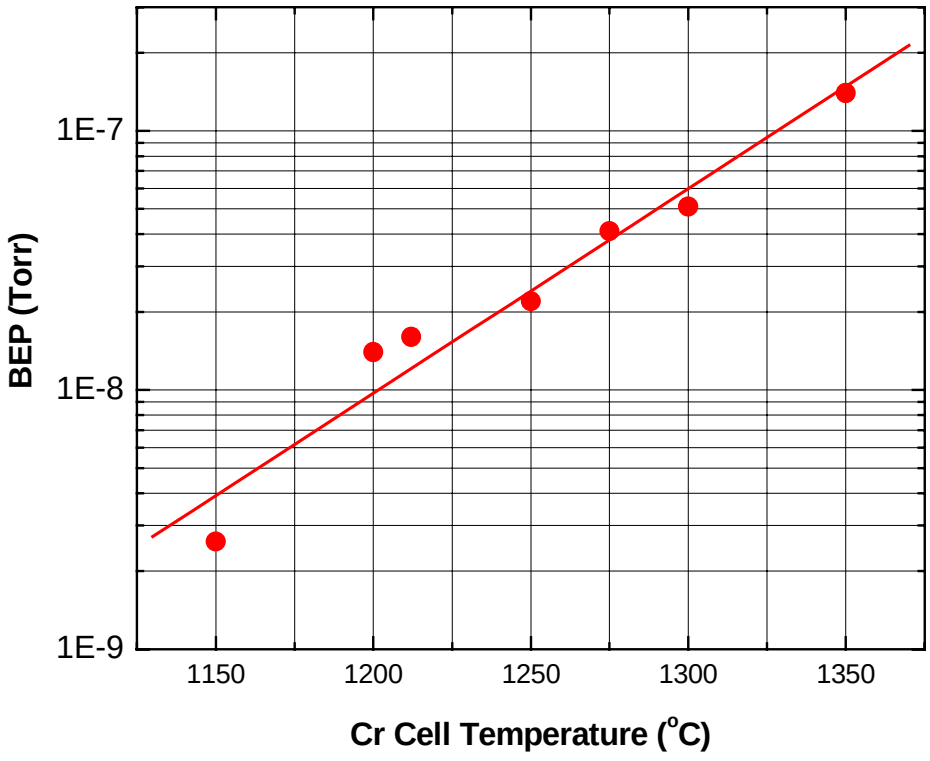

Fig 5-9. Cr BEP as a function of K-cell temperature. The BEP is plotted in log scale.

It can be seen that the nominal Cr concentration increases with the Cr K-cell temperature as shown in Fig 5-10. Saito *et al.* has reported room temperature ferromagnetism for

$Zn_{1-x}Cr_xTe$ with x = 0.2 [4]. We estimated that 20% Cr doping concentration could be realized when the Cr K-cell temperature is about 1350°C in our system.

Table 5-1. Relationship between Cr cell temperature and Cr/Te flux ratio and nominal Cr concentration

Cr Cell temperature(°C)	1050	1150	1175	1200	1225	1280	1300
Cr/Te flux ratio	0.00373	0.0357	0.0339	0.0797	0.0919	0.24	0.319
Nominal Cr concentration	0.25%	2.36%	2.73%	6.18%	7.06%	16.6%	17.73%

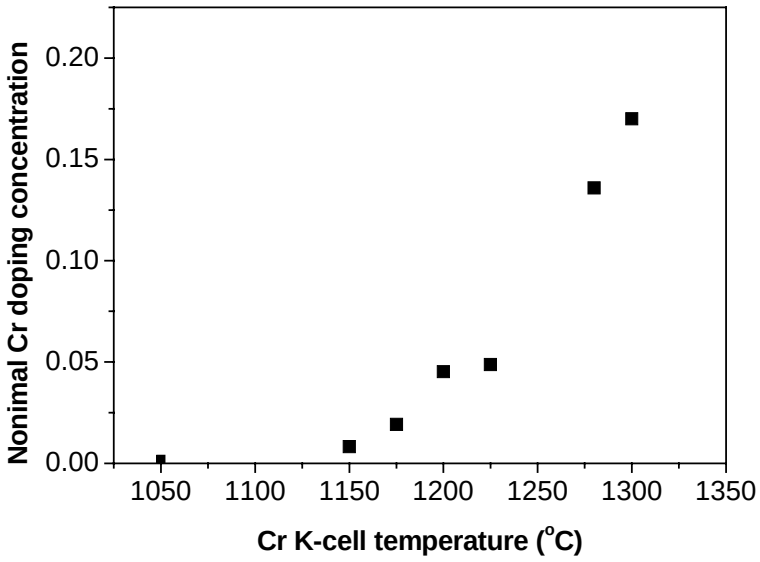

Fig 5-10. Nominal Cr concentration as a function of Cr K-cell temperature.

The substrate temperature used for all the growth was 200°C. The structural, magnetic and compositional properties of some of the samples are presented in the following sections.

5.2.1 Structural Properties

RHEED patterns showed that the surface of the sample with higher Cr K-cell temperature is rougher than that with lower Cr K-cell temperature with the same time duration of growth. Figure 5-11 shows the RHEED patterns of growths with Cr cell temperature of 1050^{o}C, 1150^{o}C, 1200^{o}C and 1300^{o}C. The streaky (2x1) RHEED patterns of the ZnTe buffer layers shows that all the buffer layers were grown with good crystal quality and could act as a virtual substrate for the growth. With the increase of growth duration, the RHEED pattern became spotty. It was observed that when the Cr K-cell temperature was set higher than 1250^{o}C, the RHEED pattern became spotty immediately after a few monolayers Cr-ZnTe deposition.

AFM measurement was also used to investigate the morphology of the samples. Figure 5-12 shows the AFM images of six samples with Cr cell temperature of 1050^{o}C, 1150^{o}C, 1175^{o}C, 1200^{o}C, 1225^{o}C and 1300^{o}C. Grains could be observed from all the samples. However the grain size did not follow any trend with the increase of the Cr K-cell temperature. Table 5-2 presents the RMS values of all the samples. The RMS value, which indicates the roughness of the film surface, did not show any obvious trend with the change of Cr K-cell temperature. It suggested that the quality of the surface might not solely depend on the Cr K-cell temperature. Thus other factors may also affect the morphology of surface, such as the stability of the source flux.

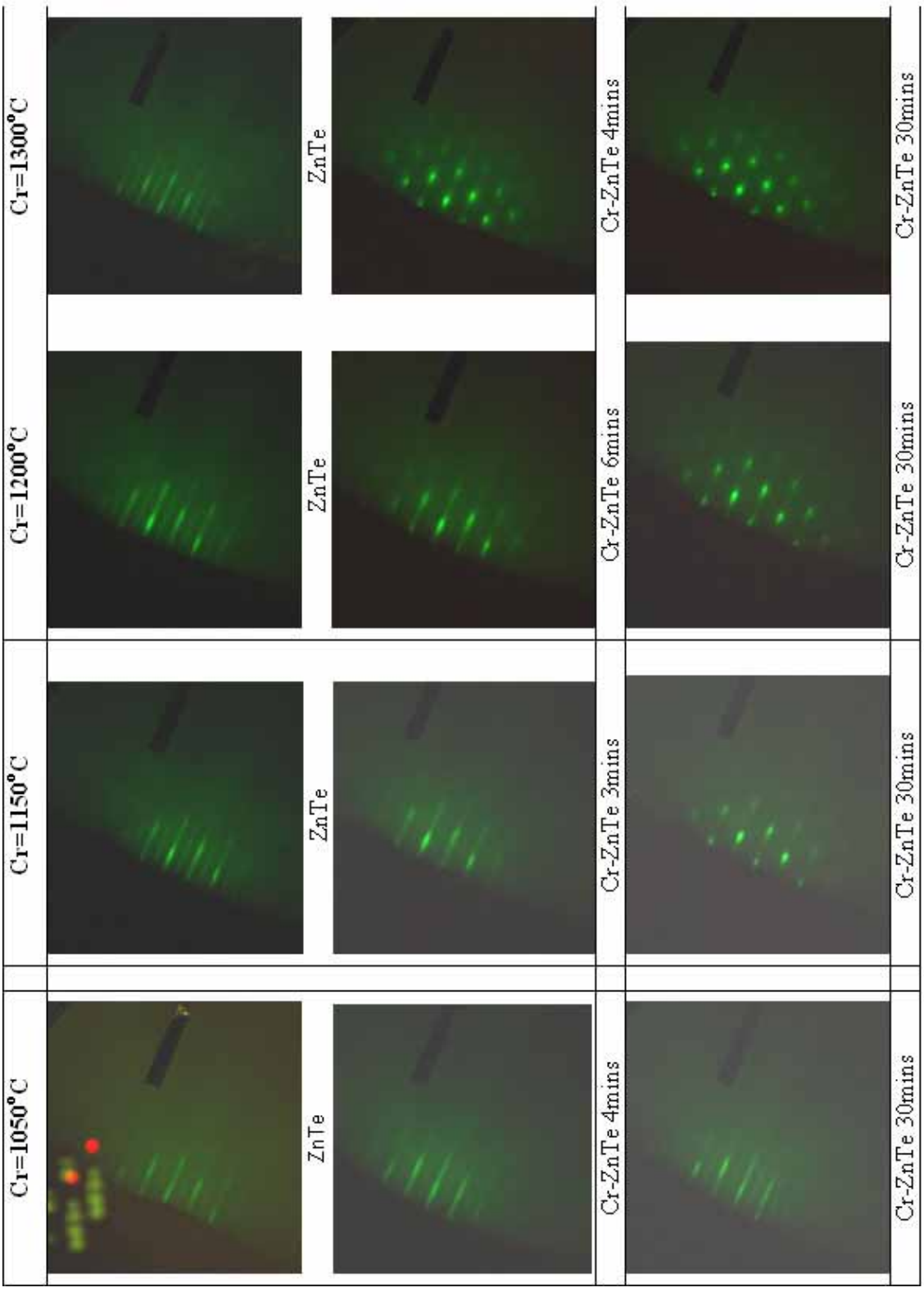

Fig 5-11. RHEED pattern with Cr K-cell temperature of 1050°C, 1150°C, 1200°C and 1300°C in $[1\bar{1}0]$ direction.

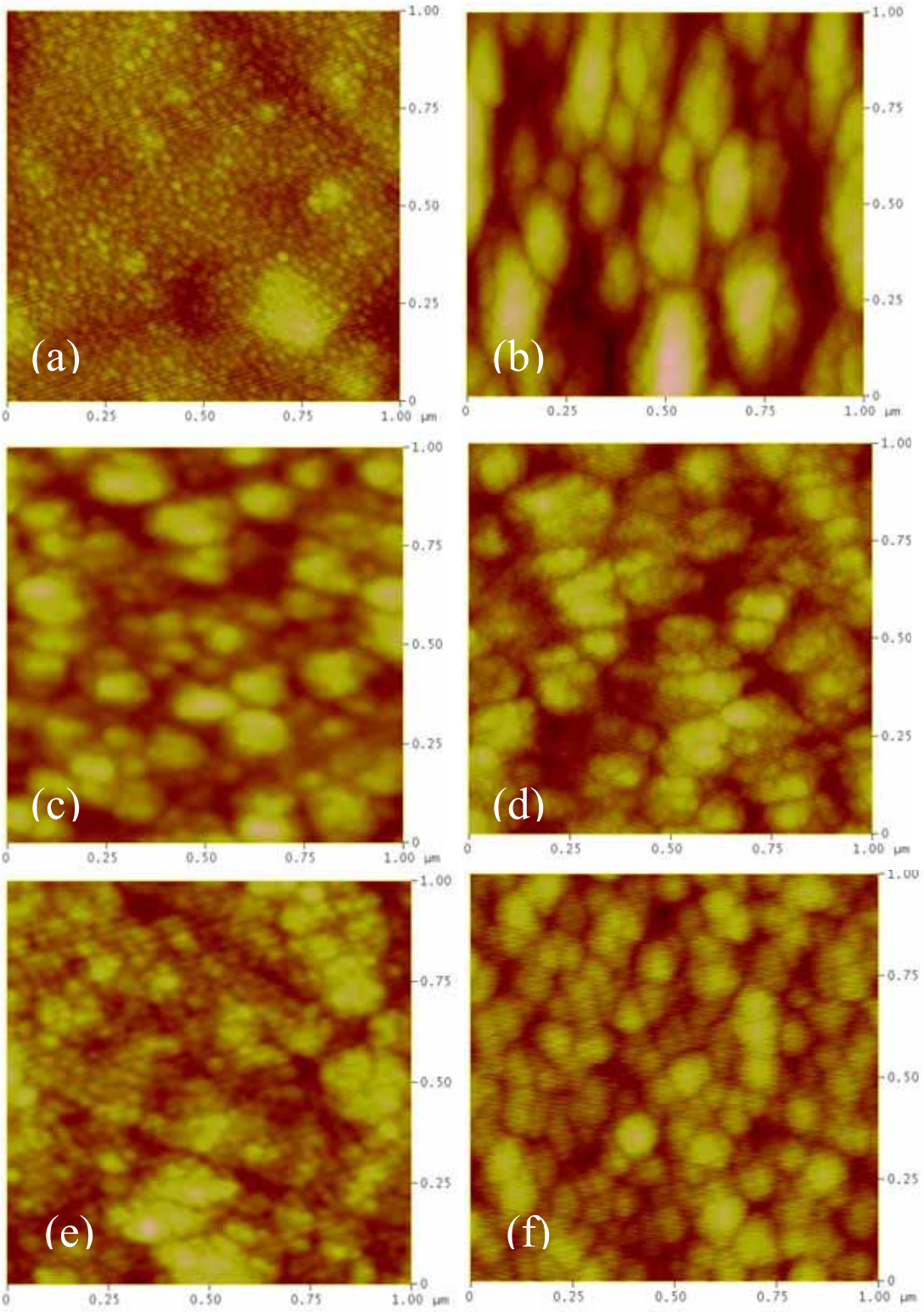

Fig 5-12. AFM images of samples with Cr cell temperature: (a) 1050°C, (b) 1150°C, (c) 1175°C, (d) 1200°C, (e) 1225°C and (f) 1300°C.

Table 5-2. RMS values of samples with different Cr cell temperature during growth

Sample No.	**S1**	**S2**	**S3**	**S4**	**S5**	**S6**	**S7**
Cr cell T	1050°C	1150°C	1175°C	1200°C	1225°C	1280°C	1300°C
RMS Value	1.826nm	6.39nm	3.343nm	5.399nm	5.581nm	5.016nm	2.32nm

XRD θ - 2θ scan were used to investigate the structure of the films. ZnTe [002] and [004] peaks can be observed clearly for all the samples. No precipitate peaks are detected in the samples. We use Bragg's law to calculate the lattice constant of our films. The equation of Bragg's law is given in equation 5-2,

$$a = \frac{\lambda}{2\sin\theta}\sqrt{h^2 + k^2 + l^2} \qquad (5\text{-}2)$$

where a is the lattice constant, λ is the wavelength of XRD system (λ ~ 1.54056Å for our system), θ is the angle where peaks are detected and h, k and l are the Miller indices. As we know, for Cr doped ZnTe DMS system, the lattice constant of the film will change if Cr substitutes Zn in the ZB crystal structure. The lattice constant change will be reflected by the shift of XRD peaks. Saito *et al.* has shown that the lattice constant would increase with the increase of Cr concentration [5] and this trend was only valid for Cr concentration less than 5% [see Fig 5-13]. However, no trend can be observed for our samples. This suggested that some of the Cr ions might not substitute Zn in the ZnTe crystal structure.

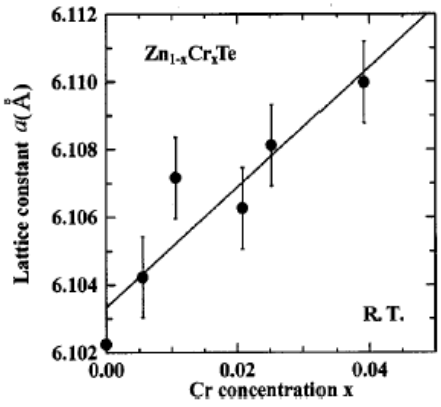

Fig 5-13. Lattice constant vs. Cr concentration from Saito *et al.* [5].

5.2.2 Cr concentration

The Cr concentration was determined by PIXE measurement. Three samples were selected and the Cr doping concentration was determined accurately. The measurement results are shown in Table 5-3. Comparing with the calculated nominal Cr doping concentration, the calculated concentrations are all higher than the measured results. However, the difference is about 3.5% for the three presented samples. Therefore, the calculated nominal concentration could still be a guide for design of the experimental parameters.

Table 5-3. Relationship between Cr K-cell temperature and Cr concentration

Sample No.	**S4**	**S5**	**S7**
Cr Cell temperature(^{o}C)	1200	1225	1300
Cr concentration from PIXE	**2.6%**	**3.5%**	**14%**
Nominal Cr concentration	6.18%	7.06%	17.73%

5.2.3 Magnetic Properties

The magnetic properties of the samples were measured by both VSM and SQUID measurement. In this section, we concentrate on three samples, whose Cr doping concentrations were determined by PIXE as 2.6%, 3.5% and 14%.

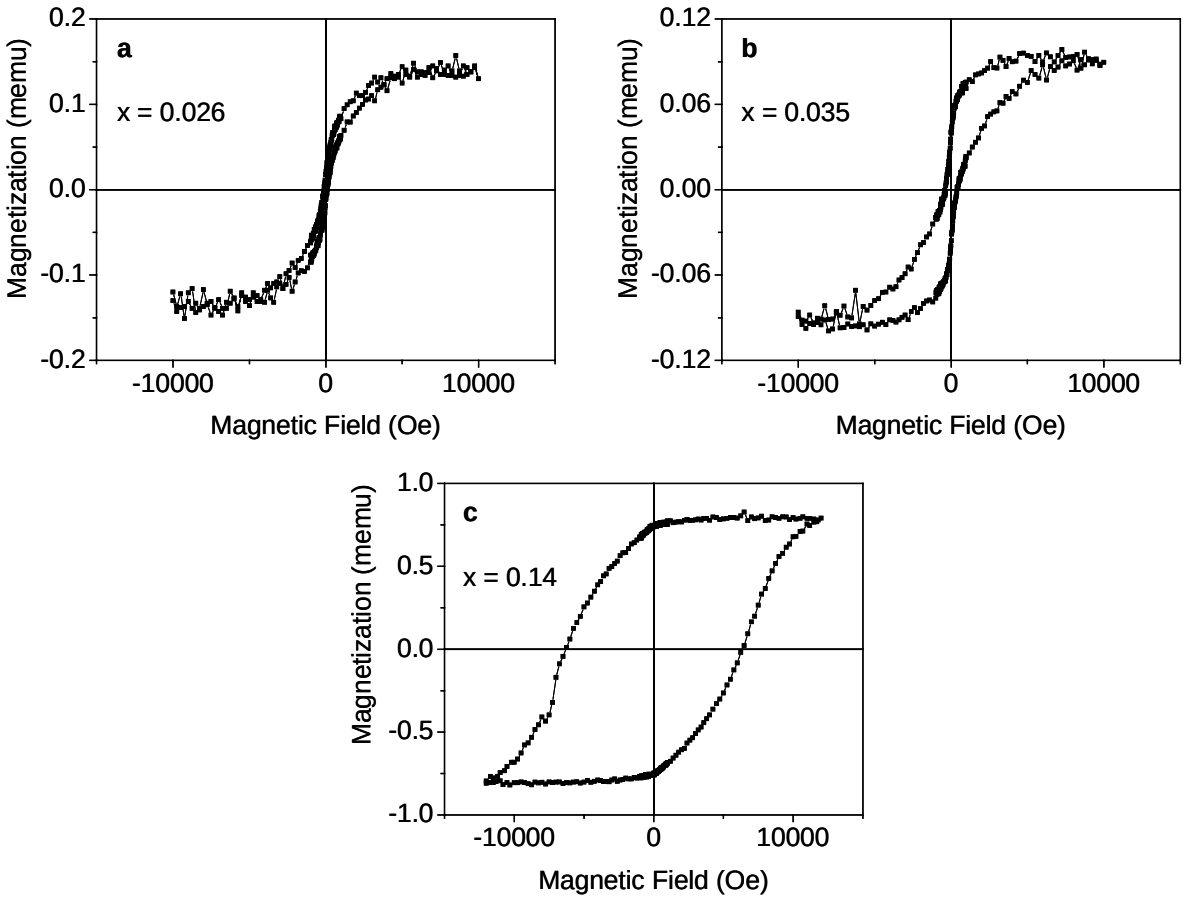

Fig 5-14. VSM measurement taken at 100K for samples with Cr doping concentration (a) x = 0.026, (b) x = 0.035 and (c) x = 0.14.

VSM measurement at room temperature showed no ferromagnetic properties for these samples. This suggests that their T_c could be lower than room temperature. At 100K,

hysteresis loops were observed clearly as shown in Fig 5-14. It was observed that the coercivity of the M-H loop increased with the Cr doping concentration. This suggests that the magnetic property was enhanced with more Cr ions doping.

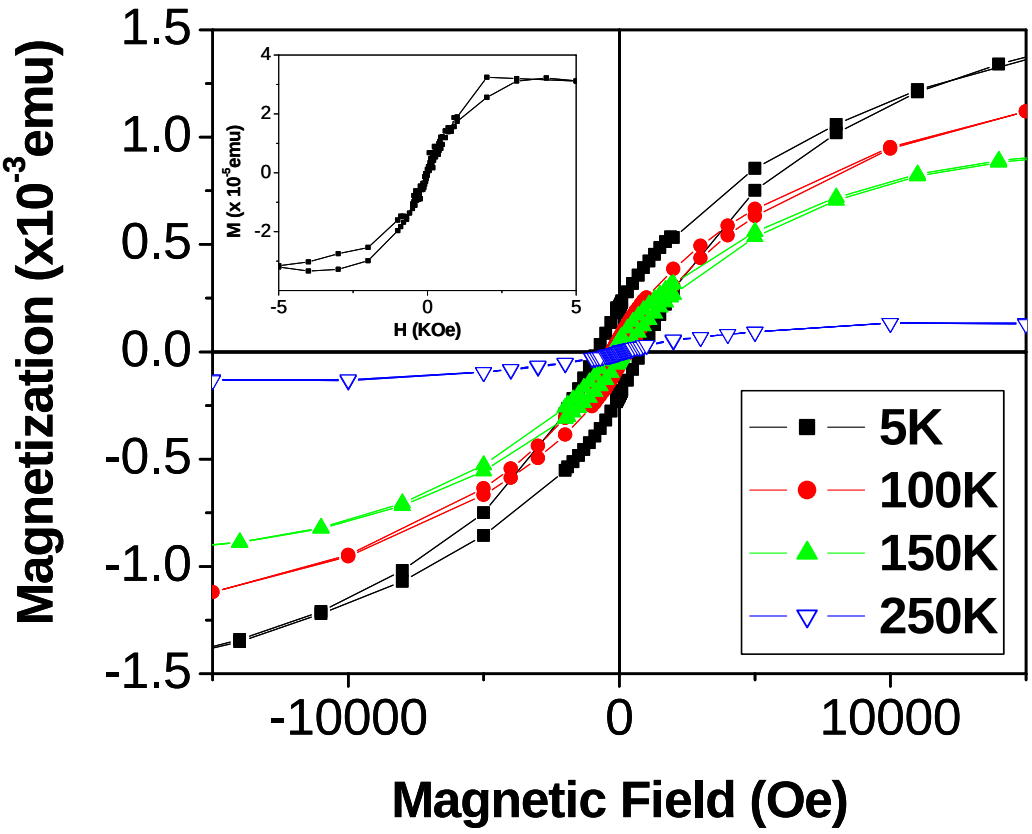

Fig 5-15. M-H hysteresis loop for sample with Cr K-cell temperature at 1350°C. The measurement was done under 5K, 100K, 150K and 250K. The inset shows the magnified M-H loop at 250K.

VSM provides a quick check whether a particular sample possesses magnetic properties. On the other hand, SQUID measurement gives us more accurate results related to the magnetic properties due to its high sensitivity and the ability to perform measurements at low temperature. Figure 5-15 shows the M-H loops measured by SQUID from 5K to

250K and its inset shows the magnified M-H curve measured at 250K; indicating T_c of this sample could be around 250K.

We fitted our results to the Curie-Weiss law in order to estimate the T_c of the samples more accurately. Temperature dependency of magnetization (M-T curve) was obtained through SQUID measurement; then the temperature dependent susceptibility curve (χ – T) and inverse susceptibility curve ($1/\chi$ – T) were deduced from the M-T curve according to the relationship χ = M/H. The T_c could be estimated by linearly fitting the high temperature portion of the $1/\chi$ – T curve as shown in Fig 5-16(a) – (c). Table 5- 4 shows the tabulated T_c with respect to their Cr K-cell temperatures and their Cr doping concentration. A T_c of ~158K was estimated for the sample with Cr concentration of 0.026 [See Fig. 5-16(a)]. The SQUID measurement showed hysteresis loop at 120K for this sample [see the inset of Fig 5-16(a)], which suggested the T_c of this sample could be higher than 120K. It shows that our estimation through fitting to the Curie-Weiss law is valid. Accordingly, the T_c of ~185K [see Fig 5-16(b)] and T_c of ~265K [see Fig 5-16(b)] were estimated for sample with Cr concentration of 0.035 and Cr concentration of 0.14, respectively.

Table 5-4. Relationship between Cr cell temperature and Curie temperature

Sample No.	**S4**	**S5**	**S7**
Cr Concentration	2.6%	3.5%	14%
Curie Temperature T_c	158K	185K	265K

It can be observed in Fig 5-16(a)-(c) that the $\chi - T$ curve shows convex shape for both Cr doping concentration of 0.035 [see Fig 5-16(b)] and 0.14 [see Fig 5-16(c)], which are generally following the Weiss mean-field theory. However, the $\chi - T$ curve is concave for the sample with Cr doping concentration of 0.026. Similar concave shape of $\chi - T$ curve has been observed in other DMS systems [6, 7]. This concave shape has often been used as an indication of localization in the presence of disorder [8, 9]. It suggests the exchange interactions inside this sample may not be homogeneous. However, when we try to fit the $1/\chi - T$ curve to the Curie-Weiss law, the fitting line intersects the temperature axis at the positive side, which indicates that the dominant magnetic interaction between Cr ions inside Cr doped ZnTe is ferromagnetic. The same conclusion has been drawn for Cr doped GaAs system [6].

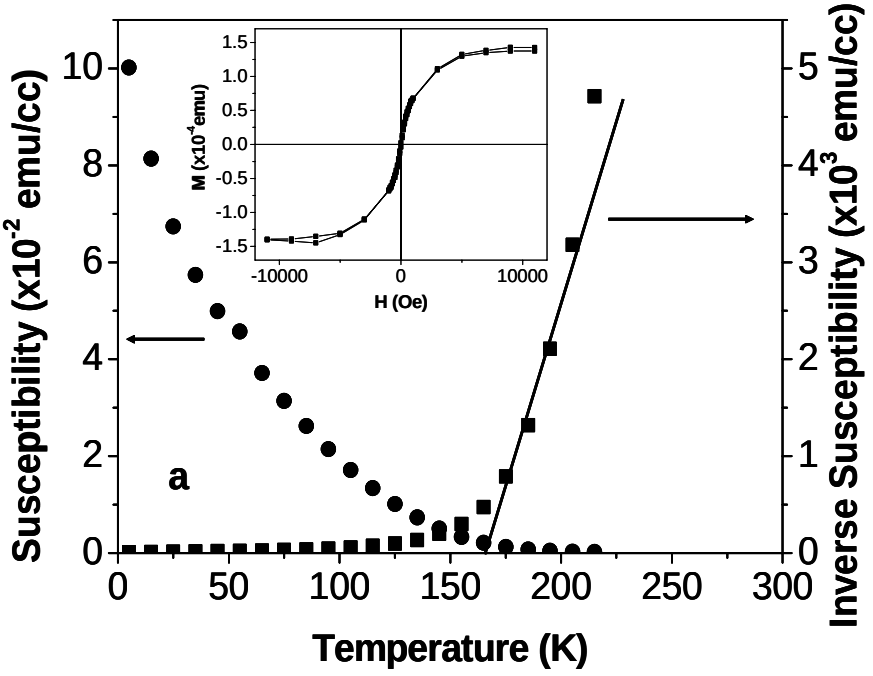

Fig 5-16(a). Temperature dependent susceptibility (χ – T) and inverse susceptibility (1/χ – T) curves for sample with *x* = 0.026. The inset shows the M-H curve at 120K.

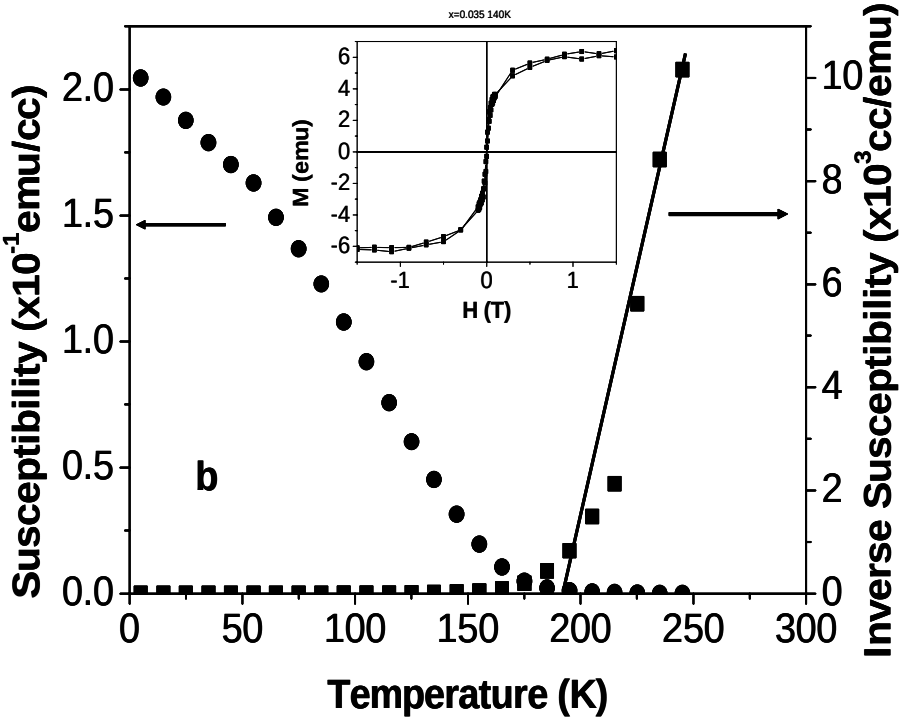

Fig 5-16(b). Temperature dependent susceptibility (χ – T) and inverse susceptibility (1/χ – T) curves for sample with *x* = 0.035. The inset shows the M-H curve at 140K.

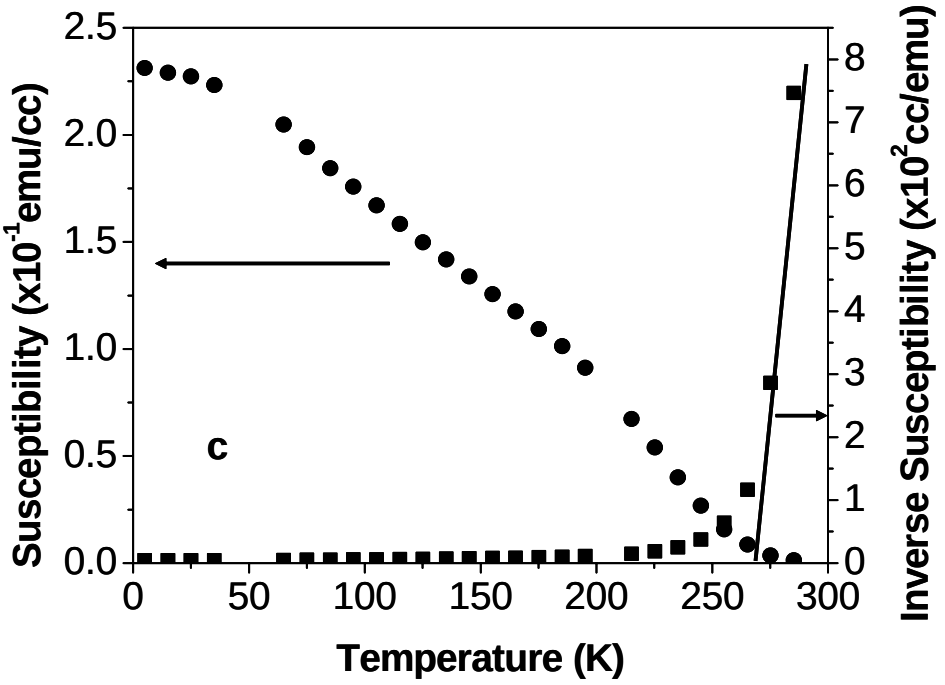

Fig 5-16(c). Temperature dependent susceptibility (χ – T) and inverse susceptibility (1/χ – T) curves for sample with *x* = 0.14.

Figure 5-17 presents the relationship between T_c and Cr-doping concentration. All the known data from literature [4-5, 13-16] as well as our own results are plotted. We can observe a linear relationship between T_c and Cr concentration. The T_c = 300K with *x* of 0.2 has been reported by Saito *et al.* [16] and T_c = 275K with *x* of 0.17 has been reported by Ozaki *et al.* [14, 15]. We see that the two data points are almost on the extension of our linear fitted line. This suggests that our results are consistent with their results. However, Saito *et al.* has also reported $T_c \sim$ 15K for x = 0.035, but we estimated $T_c \sim$ 185K for our sample with *x* of 0.035 by fitting the results to the Curie-Weiss law. Further M-H measurement with SQUID at 140K shows clear hysteresis loop [see the inset of Fig 5-17] indicating that the ferromagnetism of our sample persists at least up to 140K.

Therefore the T_c for our sample with Cr doping concentration of 0.035 should be higher than 140K.

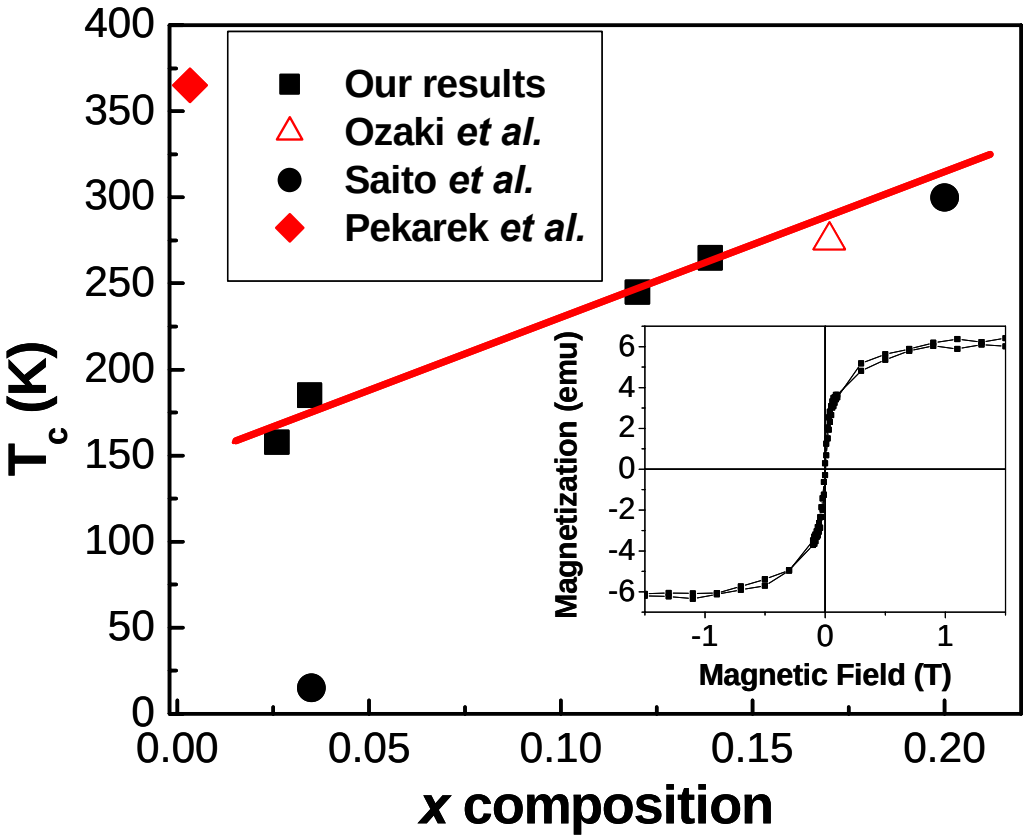

Fig 5-17. Curie temperature as a function of Cr concentration in $Zn_{1-x}Cr_xTe$ sample. A comparison of results with other groups also given [4-5, 13-16].

5.3 $Cr_{1-\delta}Te$ Precipitate Analysis

The existence of $Cr_{1-\delta}Te$ inside the grown samples is a hurdle for $Zn_{1-x}Cr_xTe$ DMS growth. $Cr_{1-\delta}Te$ is a very complex system, in which various phases have been discovered [3, 17-22]. According to the literature [3], CrTe is ferromagnetic, with Curie temperature between 180K and 340K, and has metallic conductivity. The Curie temperature for

different $Cr_{1-\delta}Te$ phases has been measured. With $\delta>0.1$, $Cr_{1-\delta}Te$ has hexagonal structure and its T_c is about 354K; with $\delta=0.25$, Cr_3Te_4 is in the structure of monoclinic and its T_c is from 315K to 340K; with $\delta=0.33$, Cr_2Te_3 has structure of trigonal and the Curie temperature is around 170K to 180K. Trigonal Cr_5Te_8 is reported to have Curie temperature of 220K [19] or 265K [20] and monoclinic Cr_5Te_8 has T_c of 220K [19] or 190K [20]. The literature survey shows that we had to pay attention to the existence of $Cr_{1-\delta}Te$ precipitates since it can exist with so many different phases.

As predicted in the beginning of section 5.2, 20% of Cr doping concentration might be realized when the Cr K-cell temperature was 1350°C. A growth was done according to this prediction with substrate temperature of 250°C and Cr K-cell temperature of 1350°C. The T_c = 365K was estimated for this sample according to M-T measurements. The group by Pekarek *et al.* has also reported T_c = 365K for their bulk $Zn_{1-x}Cr_xTe$ sample grown by vertical Bridgman method [13]. It was possible that we have obtained the same material as them. The results for this particular sample were presented in the following sections.

5.3.1 Structural Properties

Figure 5-18 shows the RHEED patterns for this particular sample. The RHEED pattern showed that the surface of the sample were quite flat since the RHEED patterns were very streaky at the end of the growth. However, comparing with the ZnTe's RHEED pattern, the spacing between the streaky lines had changed. This indicated that the $Zn_{1-x}Cr_xTe$ layers might grow in a different kind of crystal structure.

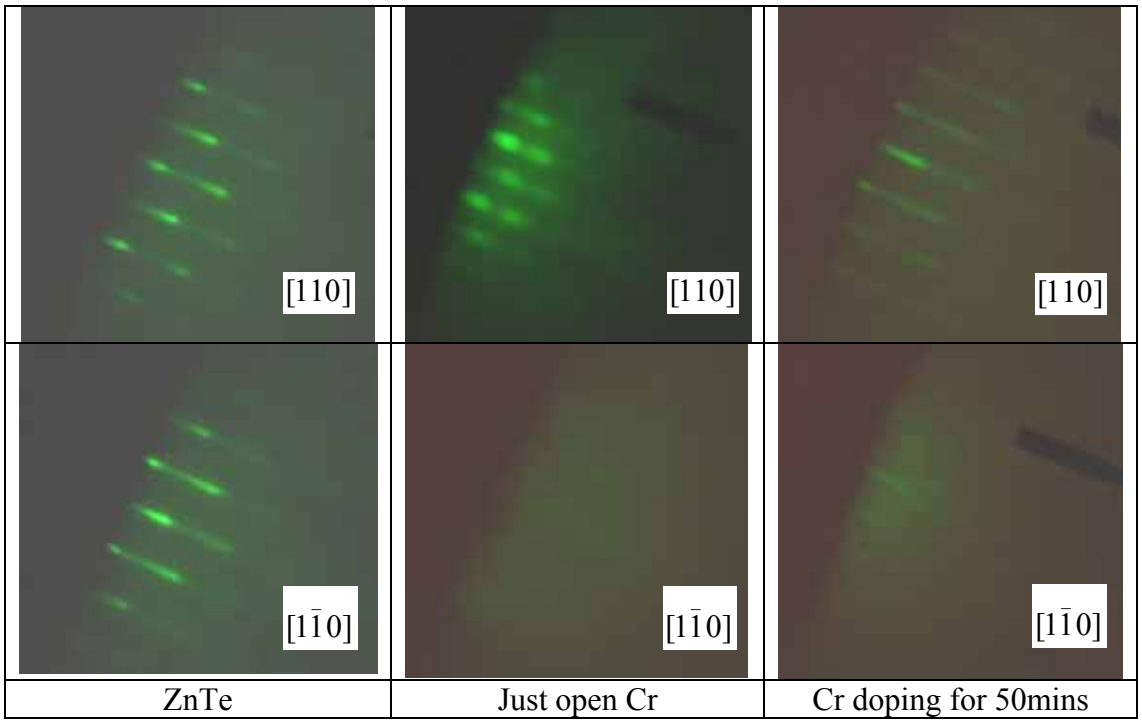

Fig 5-18. RHEED pattern for high Cr K-cell temperature growth.

The AFM measurement confirmed that the film has quite smooth surface. The RMS roughness value was 1.713nm, which was quite small comparing with other samples. The 3-D AFM scan [see Fig 5-19(b]] shows a lot of longitudinal grains forming on the surface of the sample. All the grains were almost orientated in one direction. Strong anisotropy magnetic property was predicted for this sample. In addition, SEM measurement showed that the there were a lot of clusters on the surface of the film, which was shown in Fig 5-20. The clusters were shown as bright spots in the image magnified by 5000 times. This suggests that those clusters might be very conductive. It was suspected that those clusters were $Cr_{1-\delta}Te$ since $Cr_{1-\delta}Te$ was metallic. From the image magnified by 15000 times [see Fig 5-20 (b)], we could observe that those clusters might not be clusters on the surface. They could root inside the film.

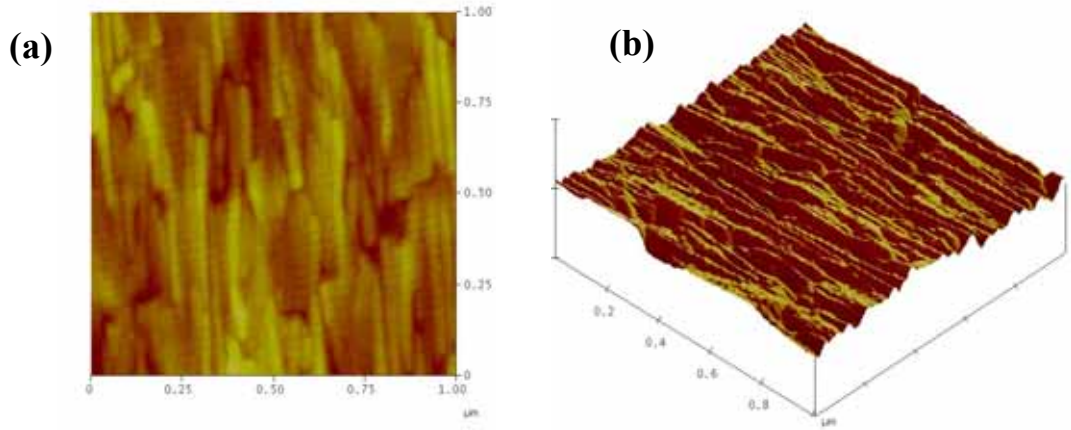

Fig 5-19. AFM measurement results. (a) AFM image of 1μm×1μm area and (b) 3D topography of 1μm×1μm area.

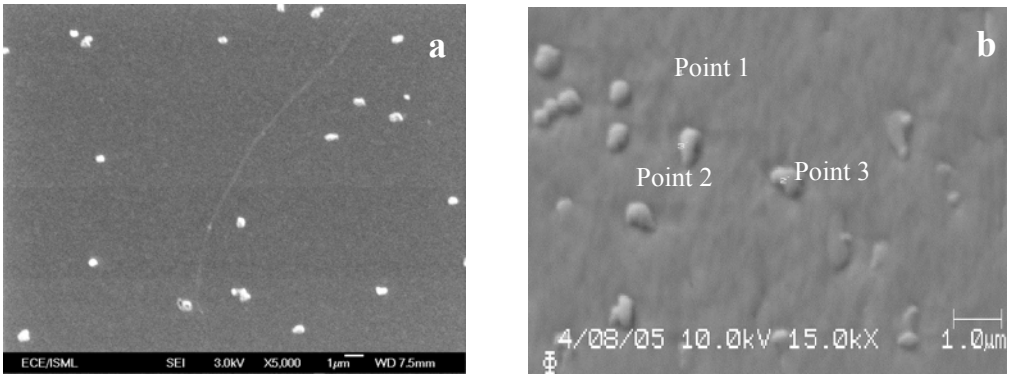

Fig 5-20. (a) SEM image, magnified by 5000 times and (b) AES image, magnified by 15000 times.

Furthermore, XRD 2-θ scan was carried out and three different peaks were found besides the ZnTe and GaAs peaks [See Fig 5-21]. 2θ = 38.63, 39.21 and 44.30 which could not be identified. We suspected that those unknown peaks might correspond to $Cr_{1-\delta}Te$ precipitates.

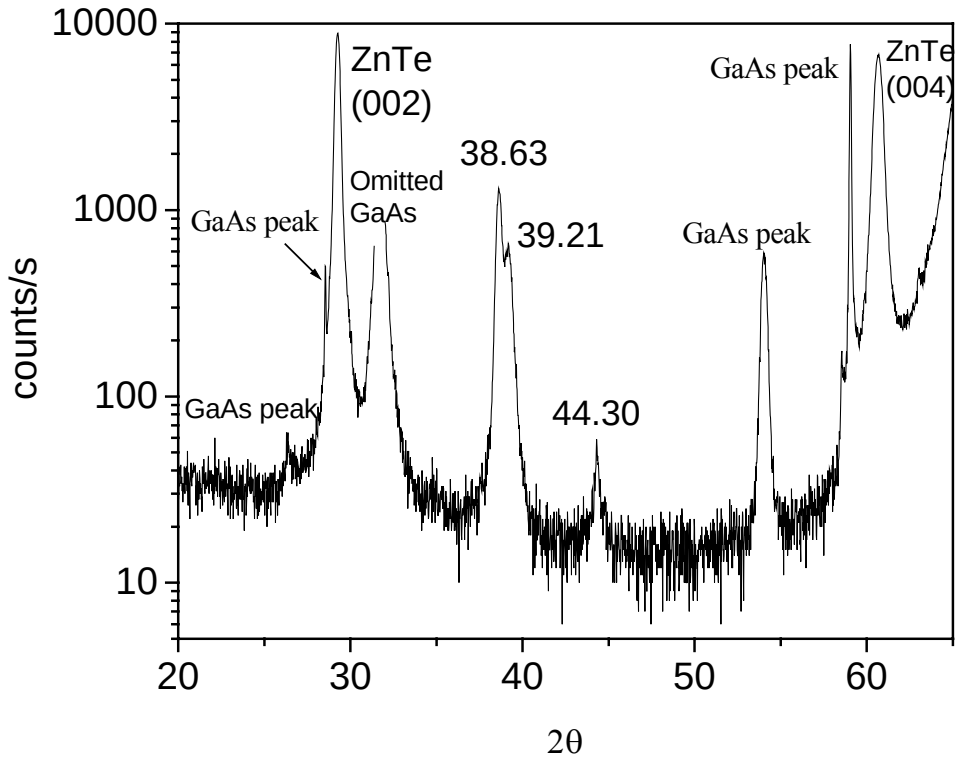

Fig 5-21. XRD θ-2θ scan for the high Cr doped sample. The GaAs peak refers to peaks generated by other wavelength X-ray.

5.3.2 Cr concentration

EDX and AES measurements were carried out to check the composition of the film. Figure 5-22 shows the SEM picture taken during EDX measurement and Table 5-5 shows the concentrations of elements in this sample. It was found that the Cr concentration of the cluster (Spectrum 2) was higher than that of the normal film (Spectrum 1). This result confirmed our previous suspicion that the clusters observed on the surface of the film could be $Cr_{1-\delta}Te$ precipitates.

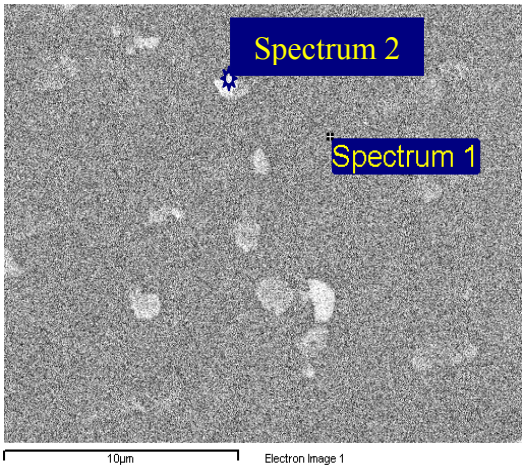

Fig 5-22. SEM measurement. Two points were measured. Spectrum 2 was measured on the cluster and spectrum 1 was measured on the normal film.

Table 5-5. EDX measurement results. Comparison of composition of spectrum 1 and 2

Element	Spectrum 1	Spectrum 2
C K	48.68%	43.98%
O K	33.97%	29.00%
Cr K	**6.76%**	**17.59%**
Te L	10.58%	9.43%

Auger Electron Spectroscopy (AES) measurements also proved that there was no Zn element in this sample. Only Cr, Te and O were observed during the measurement. Therefore we can confirm that Zn was unable to incorporate into the sample and probably only $Cr_{1-\delta}Te$ was grown in this particular growth.

5.3.3 Magnetic Properties

From the VSM and SQUID measurements, a very strong magnetic signal is detected for this particular sample. Figure 5-23 shows the VSM results measured from room temperature to 370K. The coercivity (Hc) and saturated magnetization (M_s) decrease with increasing temperature. However, a weak hysteresis loop could still be observed at 370K. The inset of Fig 5-23 shows the magnified results. This suggests that the T_c of this sample could be around 370K.

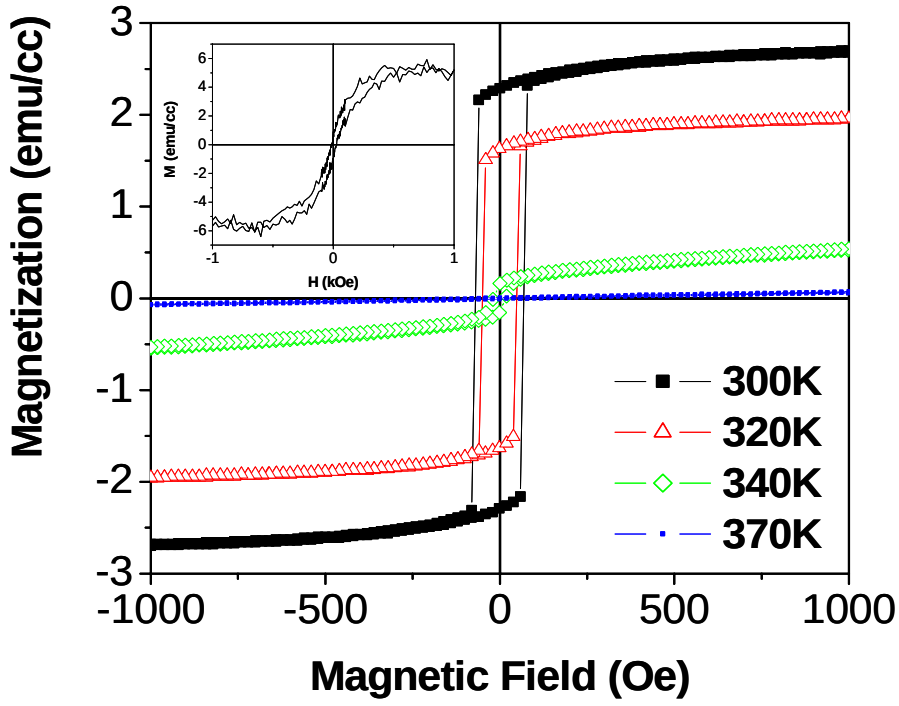

Fig 5-23. VSM measurements for the highly Cr-doped sample at 300K, 320K, 340K and 370K. The inset shows the magnified M-H curve at 370K.

Figure 5-24 shows the temperature dependence of magnetization (M-T) investigated through SQUID measurement with magnetic field of 100Oe and 10kOe applied parallel

to the sample surface. The inset of Fig 5-24 shows the temperature dependent inverse-susceptibility ($1/\chi$ - T) curve. The T_c for this highly doped sample was estimated to be 365K through the fitting of the inverse-susceptibility versus temperature ($1/\chi$ - T) curve to the Curie-Weis law [See the inset of Fig 5-24].

The cusp-like M-T curves were observed for both high field (H = 10kOe) and low field (H = 100Oe) measurements. A transition temperature of about 100K could be identified for the 100Oe measurement. Through a thorough literature survey, it is found this transition temperature corresponds to the transition temperature of monoclinic Cr_3Te_4 [3], at which a change from a canted ferromagnetic state to a collinear ferromagnetic state happened for monoclinic Cr_3Te_4. The literature also shows the T_c for this Cr_3Te_4 precipitate is ~ 361K [24], which is quite close to the 365K that we have obtained. It is possible that the ferromagnetism observed in this high Cr doped sample could be due to monoclinic Cr_3Te_4 precipitates inside the film. We also observe that the transition temperature shifts from 100K to 75 K when the applied field changes from 100Oe to 10kOe. The shift of this transition temperature is due to the fact that with higher magnetic field applied, most of the magnetic moments in this sample are orientated in the same direction of the field. Therefore the transition from canted ferromagnetic state to a collinear ferromagnetic state would happen at a lower temperature.

Furthermore, the saturated magnetization is about 340emu/cc at 5K from the M-T curve, which is quite large comparing to 44 emu/cc of InMnAs [25] and ~ 10 emu/cc of $Zn_{0.965}Cr_{0.035}Te$ [5]. This supports our suspicion that the strong magnetism may not come

from $Zn_{1-x}Cr_xTe$ DMS. Pekarek *et al.*, has reported bulk $Zn_{1-x}Cr_xTe$ samples with T_c of 365K, which were prepared using vertical Bridgman method [13]. It is possible that we have obtained the same material as Pekarek *et al.*. Pekarek *et al.* has suggested the possibility of $Zn_xCr_yTe_z$ or $Cr_{1-\delta}Te$ precipitates, which is responsible for the high T_c obtained. As mentioned in the previous section, no trace of Zn particles was detected in the EDX and AES measurements for this highly Cr-doped sample. Therefore, we could conclude that the strong ferromagnetism observed in highly Cr-doped samples could be due to Cr_3Te_4 precipitate, which has a transition temperature at around 100K and T_c ~ 365K.

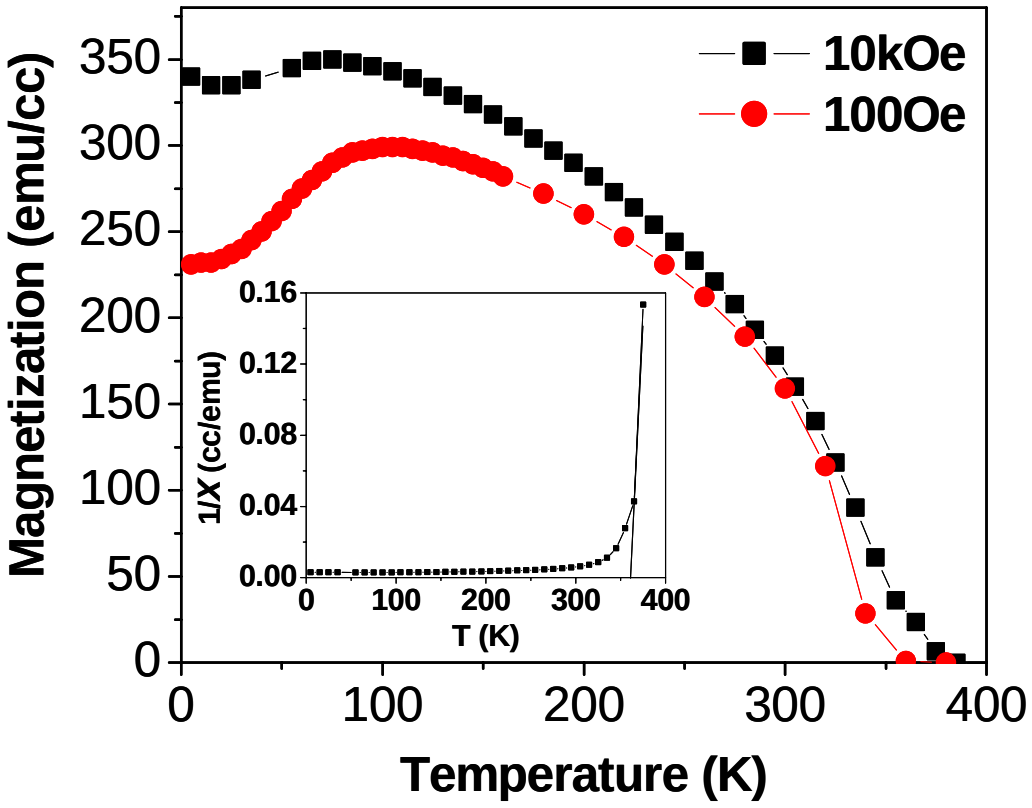

Fig 5-24. The M-T measurement for the highly Cr-doped sample measured by SQUID from 5K to 395K with applied magnetic field of 100 Oe and 10 KOe. The inset shows the 1/χ-T curve.

Field cooling (FC) and zero field cooling (ZFC) M-T measurements were also performed for the same sample under both low and high magnetic field. During the measurement, the sample was put inside the SQUID system at room temperature. A positive magnetic field was applied in order to center the sample. The magnetic field was brought to zero followed by the cooling down of the SQUID system. When the temperature reached 5K, magnetic field was applied to the sample in order to do the measurement. The temperature then swept from 5K to 400K. The magnetization of the sample was measured at different temperature. At 400K, the magnetization of the sample disappeared. After this, the sample was cooled down again from 400K to 5K with the magnetic field applied continuously for the FC measurement. After the sample was cooled down to 5K, measurement was done again at different temperature. A re-measurement for the same sample has been done and similar M-T curve was observed.

The FC-ZFC M-T curves were shown in Fig 5-25.

From Fig 5-25, it could be observed the ZFC M-T curve was almost the reciprocal of FC M-T curve at temperature below ~260K with 100Oe magnetic field applied for measurement. The ZFC measurement showed negative magnetization from 5K till ~ 260K. At 270K the magnetization suddenly became positive. From 280K onwards, the FC and ZFC curves were overlapped till 400K. However, the FC-ZFC M-T measurement shows that the positive magnetization and the FC and ZFC curves were almost the same for the measurement with 10kOe magnetic field applied. The magnetization disappeared at about 360K for 100Oe magnetic field and the magnetization only disappeared at about 380K for measurement with 10kOe magnetic field applied.

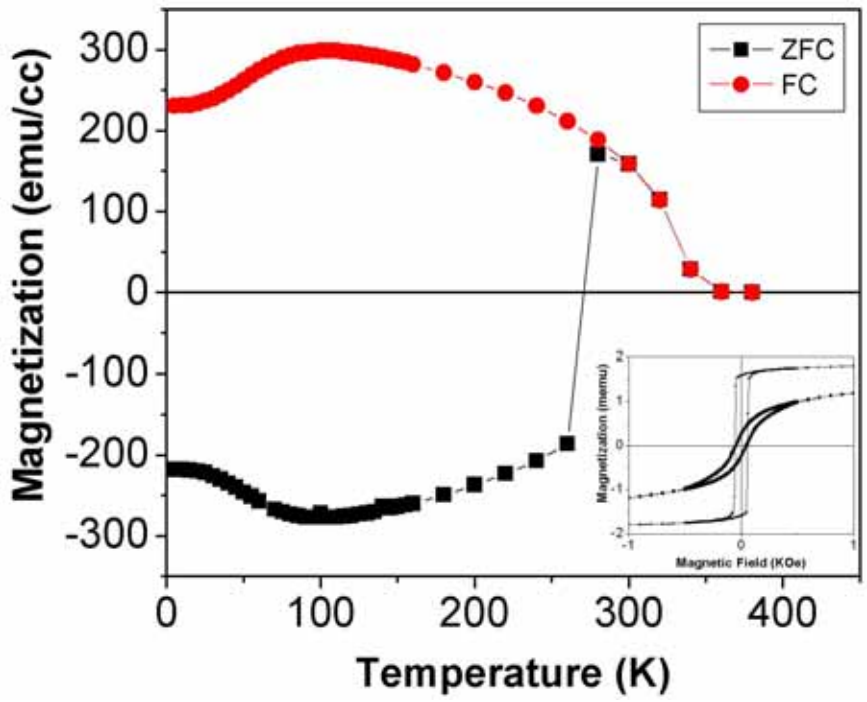

Fig 5-25. FC & ZFC M-T measurement by SQUID from 5K to 400K. 100Oe magnetic field was used. The inset is the hysteresis loop measured by VSM at room temperature. The magnetic field was applied in plane and perpendicular to each other for the two hysteresis loops measured.

When we correlate this observation with the AFM images obtained in the previous section, one of the possible reasons for the negative valued ZFC M-T curve from 100Oe field measurement could be due to the anisotropic effect. Since the grains of this film were all orientated in one direction, the magnetization of the film might be oriented easily in one direction. After centering of the sample before the SQUID measurement started, the magnetic field was brought to zero. However, there could be a negative magnetic field still present when we brought the magnetic field to zero. During ZFC cooling process, the negative magnetic field could magnetize the sample into its direction. Therefore, negative magnetization was detected when the temperature was very low. At low temperature, the coercivity of the sample was high. With the increase of the temperature, the coercivity of the sample decreased till smaller than 100Oe at the

temperature range of 260K to 270K. Then the applied 100Oe magnetic field is able to switch the magnetization of the sample into the positive direction. Therefore, positive magnetization was observed from ~270K. When the temperature was raised to 400K, the magnetic momentum of the sample is randomly distributed since there is no magnetic property observed. In the FC measurement, the magnetization of the film was slowly orientated to the direction of the applied 100Oe magnetic field during the cooling process. Therefore, positive magnetization was observed for the FC measurement for all the time. For high field FC-ZFC measurement, the field was strong enough to overcome the coercivity of the sample and orientate the magnetization of the film along the direction of the applied field. Recently, more experiment have been conducted to check that indeed there is no difference in the FC and ZFC curves (all positive values) for high field ZFC-FC measurement. We further conducted another experiment. Two M-H measurements were performed by VSM with magnetic field applied in plane but perpendicular to each other. The M-H curves showed anisotropy property [see the inset of Fig 5-25]. This supports our explanation that the sample has high anisotropy. Similar negative ZFC-FC curve has also been observed in CrTe/ZnTe/GaAs sample. [26] However, when magnetic field was applied perpendicular to the previous magnetic field direction (still in plane with the sample surface), no negative ZFC curve was observed with 100Oe magnetic field. This suggest when the magnetic field was applied not in the easy axis of the sample, the 100Oe was able to magnetize the sample in the field's direction. This further supported our explanation that the negative ZFC M-T curve was due to the anisotropy property of the sample.

In summary, we would like to attribute the observed strong ferromagnetism of this highly Cr doped ZnTe sample to be due to monoclinic Cr_3Te_4. This also suggests that other phase of $Cr_{1-\delta}Te$ precipitates besides NiAs $Cr_{1-\delta}Te$ should be considered in the study of the Cr doped ZnTe system.

Reference:

[1] Powder Diffraction File [electronic resource]: PDF-2database.

[2] http://www.webelements.com/webelements/elements/text/periodic-table/key.html

[3] J Dijkstra, H H Weitering, C F van Brugger, C Haas and R A de Groot, J. Phys.: Condens. Matter **1**, 9141 (1989).

[4] H. Saito, V. Zayets, S. Yamagata, and K. Ando, Phys. Rev. Lett. **90** (2003) 207202.

[5] H. Saito, V. Zayets, S. Yamagata, and K. Ando, Phys. Rev. B **66**, 081201(2002).

[6] H. Saito, W. Zaets, R. Akimoto and K. Ando, J. Appl. Phys. **89**, 7392 (2001).

[7] A. Van Esch *et al.*, Phys. Rev. B **56**, 13103 (1996).

[8] V. I. Litvinov and V. K. Dugaev, Phys. Rev. Lett. **86**, 5593 (2001).

[9] M. Berciu and R. N. Bhatt, Phys. Rev. Lett. **87**, 107203 (2001).

[10] Y. D. Park, A. T. Hanbicki, S. C. Erwin, C. S. Hellberg, J. M. Sullivan, J. E. Mattson, T. F. Ambrose, A. Wilson, G. Spanos, and B. T. Jonker, Science **295**, 651 (2002).

[11] A. Van Esch *et al*., Phys. Rev. B **56**, 13103 (1996).

[12] W. Bensch, O. Helmer and C. Nather, Materials Research Bulletin **32**, 305 (1997).

[13] T. M. Pekarek, D. J. Arenas, B. C. Crooker, I. Miotkowski and A. K. Ramdas, J. Appl. Phys. **95**, 7178 (2004).

[14] N. Ozaki, N Nishizawa, S Kuroda and K Takita, J. Phys.: Condens. Matter **16**, s5773 (2004).

[15] N. Ozaki, N. Nishizawa, S. Marcet, S Kuroda and K Takita, J. Superconductivity: Incorporating Novel Magnetism **18**, 29 (2005).

[16] H. Saito, V. Zayets, S. Yamagata, and K. Ando, J. Appl. Phys. **93**, 6796 (2003).

[17] H. Ipser, K.L. Komarek, K.O. Klepp, J. Less-Common Met **92**, 265 (1983).

[18] T. Hashimoto, M. Yamaguchi, J. Phys. Soc. Jpn. **27**, 1121 (1969).

[19] K. Shimada, T. Saitoh, H. Namatame, A. Fujimori, S. Ishida, S. Asano, M. Matoba, and S. Anzai, Phys. Rev. B **53**, 7673 (1996).

[20] K. Lukoschus, S. Kraschinski, C. Nather, W. Bensch, and R. K. Kremerb, Journal of Solid State Chemistry **177**, 951 (2004).

[21] J. H. Zhang, T. L. T. Birdwhistell, C. J. O'Connor, Solid State Commun. **74**, 443 (1990).

[22] K. O. Klepp, H. Ipser, Angew. Chem. Int. Ed. Engl. **21**,911 (1982).

[23] H. Ohno, A. Shen, F. Matsukura, A. Oiwa, A. Endo, S. Katsumoto, and Y. Iye, Appl. Phys. Lett **69** (1996) 363.

[24] Takasu Hashimoto and Masuhiro Yamaguchi, J. Phys. Soc. Japan **27**, 1121 (1969).

[25] H. Munekata, H. Ohno, R. R. Ruf, R. J. Gambino, and L. L. Chang, J. Cryst. Growth **111**, 1011 (1991).

[26] Research result of NUS PHD student M. G. Sreenivasan (not published yet)

Chapter 6: Conclusion and Recommendation

This thesis consists of two main parts. The first part is MBE growth of Cr doped ZnTe thin films. The second part is to characterize the grown samples in order to investigate the structural and magnetic properties.

In this project, the growth condition for epitaxial film growth was optimized through varying the substrate temperature, Zn/Te and Cr/Te flux ratio. Proper growth conditions were established such as the Zn/Te flux ratio has to be in the range of 1.2 to 2.7 and the substrate temperature has to be 200^{o}C to 250^{o}C for high quality growth of thin films. Different Curie temperatures were achieved by varying the concentration of Cr. The structural properties of the samples were studied through observation of *in-situ* RHEED pattern and the measurements of XRD, AFM and SEM. The VSM and SQUID were used to assess the magnetic properties of the samples. The composition of the samples was measured by EDX and PIXE.

Three substrate temperatures were used for growth, namely T_s = 100^{o}C, 200^{o}C and 400^{o}C. It was found that the sample grown under T_s = 200^{o}C showed clear and spotty RHEED pattern. For the sample grown under T_s = 100^{o}C, the RHEED pattern is diffuse and the sample grown under T_s = 400^{o}C shows streaky plus spotty RHEED pattern, which was different from the ZB-structured RHEED pattern. AFM and SEM measurements also proved that sample with T_s = 200^{o}C has smaller rms roughness value than the other two samples that were grown at T_s = 100^{o}C and 400^{o}C. The XRD 2θ scan shows that the sample for T_s = 400^{o}C contains precipitate peaks indicating the possible

existence of $CrTe_3$ precipitates inside the film. The VSM measurement shows that the sample grown at T_s = 400°C has very strong magnetic momentum, but it could come from the CrTe precipitate. The other two samples did not show strong signal from the VSM measurement. The SQUID measurement shows that the sample grown at T_s = 200°C has T_c of 185K and the sample grown at T_s = 100°C has T_c = 75K. Therefore, we conclude that T_s = 200°C is the most appropriate growth temperature for Cr doped ZnTe growth.

The Cr/Te flux ratio was varied from 0.0357 to 0.89 in order to change the Cr doping concentration and hence this will affect the Curie temperature of the thin film grown. The Cr/Te flux ratio is directly related to the Cr K-cell temperature. A range of Cr K-cell temperatures from 1050°C to 1300°C were used for doping. It was found that the higher the Cr K-cell temperature, the RHEED pattern becomes more spotty easily; when the Cr K-cell temperature is higher than 1250°C the RHEED shows spotty plus ring-like pattern, which indicated that the surface becomes rougher. The VSM measurements show that some of the sample had clear hysteresis loops at 100K. The SQUID measurements show that with the increase of the Cr K-cell temperature, the Curie temperature observed from the M-T measurement also increases. This is consistent with the theoretical prediction and also confirms our assumption that higher Cr cell temperature would cause higher Cr doping concentration. The Cr concentration inside the samples was determined through PIXE measurements. From the plot of Curie temperature versus Cr concentration, a linear relationship was established. Through the extrapolation of that linear relationship, the room temperature Curie temperature could be achieved with Cr concentration of 20%.

$Cr_{1-\delta}Te$ precipitate was formed when Cr K-cell temperature was raised to 1350^{o}C. High magnetization of 340emu/cc at about 100K was found in this sample. The Curie temperature of 365K was obtained, which was higher than the reported Curie temperature of all $Cr_{1-\delta}Te$ phases. XRD shows this precipitate possibly has 2θ peaks at 38.63^{o}, 39.21^{o} and 44.30^{o}.

Several suggestions for the future work:

Hall Effect measurement shall be carried out in order to find out the electrical properties of the film. By comparing the resistivity of different samples, the shape of the curvature of M-T curves from SQUID measurement shall be studied. The purpose is to check whether convex curve corresponds to lower resistivity films and concave curve is corresponds to higher resistivity. Doping with higher Cr K-cell temperature shall be tried out with same Zn/Te flux ratio of 1.2 and 200^{o}C growth temperature. The purpose of this growth is to try whether we could realize room temperature T_c without CrTe precipitates. The growth rate shall be lowered through decreasing the Zn and Te flux. With slower growth, better structured film can be obtained since the molecules have more time to move around. Annealing could also be performed in order to improve the crystal quality because the crystal defects could be healed through annealing.

PUBLICATION

1. X. J. Hou, K. L. Teo, M. G. Sreenivasan, T. Liew and T. C. Chong, MBE Growth and Properties of Cr-doped ZnTe on GaAs (001). *in* Thin Solid Films, 505, pg 126-128, (2006).

2. M. G. Sreenivasan, X. J. Hou, K. L. Teo, M. B. A. Jalil, Y. F. Liew and T. C. Chong, Growth of CrTe Thin Films by Molecular Beam Epitaxy *in* Thin Solid Films, 505, pg 133-136, (2006).